scientific reports

Check for updates

OPEN

Electric, thermal, and thermoelectric magnetoconductivity for Weyl/multi-Weyl semimetals in planar Hall set-ups induced by the combined effects of topology and strain

Leonardo Medel[1]✉, Rahul Ghosh[2], Alberto Martín-Ruiz[1] & Ipsita Mandal[2,3]

We continue our investigation of the response tensors in planar Hall (or planar thermal Hall) configurations where a three-dimensional Weyl/multi-Weyl semimetal is subjected to the combined influence of an electric field E (and/or temperature gradient $\nabla_r T$) and an effective magnetic field B_χ, generalizing the considerations of Phys. Rev. B 108 (2023) 155132 and Physica E 159 (2024) 115914. The electromagnetic fields are oriented at a generic angle with respect to each other, thus leading to the possibility of having collinear components, which do not arise in a Hall set-up. The net effective magnetic field B_χ consists of two parts—(a) an actual/physical magnetic field B applied externally; and (b) an emergent magnetic field B_5 which quantifies the elastic deformations of the sample. B_5 is an axial pseudomagnetic field because it couples to conjugate nodal points with opposite chiralities with opposite signs. Using a semiclassical Boltzmann formalism, we derive the generic expressions for the response tensors, including the effects of the Berry curvature (BC) and the orbital magnetic moment (OMM), which arise due to a nontrivial topology of the bandstructures. We elucidate the interplay of the BC-only and the OMM-dependent parts in the longitudinal and transverse (or Hall) components of the electric, thermal, and thermoelectric response tensors. Especially, for the co-planar transverse components of the response tensors, the OMM part acts exclusively in opposition (sync) with the BC-only part for the Weyl (multi-Weyl) semimetals.

There has been an incredible amount of research work focussing on the investigations of the transport properties of semimetals, which are systems harbouring band-crossing points in the Brillouin zone (BZ). Two or more bands cross at the nodal points where the densities of states go to zero. Among the three-dimensional (3d) semimetals with twofold nodal points, the well-known examples include the Weyl semimetals (WSMs)[1,2] and the multi-Weyl semimetals (mWSMs)[3–5], whose bandstructures exhibit nontrivial topology quantified by the Berry phase. The nodal points for both the WSMs and the mWSMs are protected by the point-group symmetries of the crystal lattice[4]. In the language of the Berry curvature (BC) flux, each nodal point acts as a source or sink in the momentum space and, thus, acts as an analogue of the elusive magnetic monopole. The value of the monopole charge is equal to the Chern number arising from the Berry connection. A consequence of the Nielson-Ninomiya theorem[6], applicable for systems in an odd number of spatial dimensions, the nodal points exist in pairs, with each pair carrying Chern numbers $\pm J$. Thus, the pair acts as a source and a sink of the BC flux. Since the sign of the monopole charge is called the chirality χ of the assoiciated node, the two nodes in a pair are of opposite

[1]Instituto de Ciencias Nucleares, Universidad Nacional Autónoma de México, 04510 Ciudad de México, México. [2]Department of Physics, Shiv Nadar Institution of Eminence (SNIoE), Gautam Buddha Nagar, Uttar Pradesh 201314, India. [3]Freiburg Institute for Advanced Studies (FRIAS), University of Freiburg, D-79104 Freiburg, Germany. ✉email: leonardo.medel@correo.nucleares.unam.mx

chiralities (i.e., $\chi = \pm 1$). The values of J for Weyl (e.g., TaAs[7–9] and HgTe-class materials[10]), double-Weyl (e.g., $HgCr_2Se_4$[11] and $SrSi_2$[12,13]), and triple-Weyl nodes (e.g., transition-metal monochalcogenides[14]) are equal to one, two, and three, respectively.

Suppose we consider an experimental set-up with a WSM/mWSM semimetal subjected to an external uniform electric field $\mathbf{E}$ along the x-axis and a uniform external magnetic field $\mathbf{B}$ along the y-axis. Since $\mathbf{B}$ is perpendicular to $\mathbf{E}$, a potential difference (known as the Hall voltage) will be generated along the z-axis. This phenomenon is the well-known Hall effect. However, if we apply $\mathbf{B}$ making an angle θ with $\mathbf{E}$, where $\theta \neq \pi/2$ or $3\pi/2$, the conventional Hall voltage induced from the Lorentz force is zero along the y-axis. Nonetheless, due to nontrivial Chern numbers, a voltage difference V_{PH} appears along this direction, as shown in Fig. 1. This is known as the planar Hall effect (PHE), arising due to the chiral anomaly[15–21]. The chiral anomaly refers to the phenomenon of charge pumping from one node to its conjugate when $\mathbf{E} \cdot \mathbf{B} \neq 0$, originating from a local non-conservation of electric charge in the vicinity of an individual node, with the rate of change of the number density of chiral quasiparticles being proportional to $J(\mathbf{E} \cdot \mathbf{B})$[22,23]. The associated transport coefficients, related to this set-up, are referred to as the longitudinal magnetoconductivity (LMC) and the planar Hall conductivity (PHC), which depend on the value of θ. In an analogous set-up, we observe the planar thermal Hall effect (PTHE), where we replace the external electric field by (or add) an external temperature gradient $\boldsymbol{\nabla}_{\mathbf{r}} T$. In this scenario, too, a potential difference is induced along the y-axis due to the chiral anomaly[21,24] [cf. Fig. 1], with the response coefficients known as the longitudinal thermoelectric coefficient (LTEC) and transverse thermoelectric coefficient (TTEC). There has been a tremendous amount of efforts to determine the behaviour of these response tensors[25–40].

In a planar Hall (or thermal Hall) set-up, if a semimetal is subjected to mechanical strain, it induces elastic deformations of the material. The elastic deformations couple to the electronic degrees of freedom (i.e., quasiparticles) in such a way that they can be modelled as pseudogauge fields in the semimetals[37,41–47]. The form of these elastic gauge fields shows that they couple to the quasiparticles of the Weyl fermions with opposite chiralities with opposite signs[37,44–46,48,49]. Due to the chiral nature of the coupling between the emergent vector fields and the itinerant fermionic carriers, this provides an example of axial gauge fields in three dimensions. This is to be contrasted with the actual electromagnetic fields, which couple to all the nodes with the same sign. While a uniform pseudomagnetic field $\mathbf{B}_5$ can be generated when a WSM/mWSM nanowire is put under torsion, a pseudoelectric field $\mathbf{E}_5$ appears on dynamically stretching and compressing the crystal along an axis (which can be achieved, for example, by driving longitudinal sound waves)[46]. Direct evidence of the generation of such pseudoelectromagnetic fields in doped semimetals has been obtained in experiments[50]. In an earlier work by the two of us[38], the response tensors have been computed for WSMs and mWSMs, but neglecting the orbital magnetic moment (OMM)[51,52], which is another artifact of a nontrivial topology in the bandstructures. Although the effects of OMM were included in the computations of Ref.37, only the electric conductivity at zero temperature was studied. Hence, in this paper, we derive all the relevant electric, thermal, and thermoelectric response tensors, associated with the planar Hall and planar thermal set-ups, which constitute a complete description incorporating both the BC and the OMM.

As shown in Fig. 1, the co-planar $\mathbf{E}$ and $\mathbf{B}_\chi = \mathbf{B} + \chi\, \mathbf{B}_5$ set-ups considered here consist of a nonzero $\mathbf{B}_5$ and a nonzero $\mathbf{B}$ in the xy-plane. These two parts of the effective magnetic field $\mathbf{B}_\chi$ are oriented at the angles θ and θ_5, respectively, with respect to $\mathbf{E}$ (or $\nabla_{\mathbf{r}} T$) applied along the x-axis. In other words, $\mathbf{B} = B(\cos\theta, \sin\theta, 0)$ and $\mathbf{B}_5 = B_5(\cos\theta_5, \sin\theta_5, 0)$, where $B \equiv |\mathbf{B}|$ and $B_5 \equiv |\mathbf{B}_5|$. We consider the weak magnetic field limit with low values of B and B_5, such that the formation of the Landau levels can be ignored, and the magnetoelectric, magnetothermal, and magnetothermoelectric response can be derived using the semiclassical Boltzmann formalism.

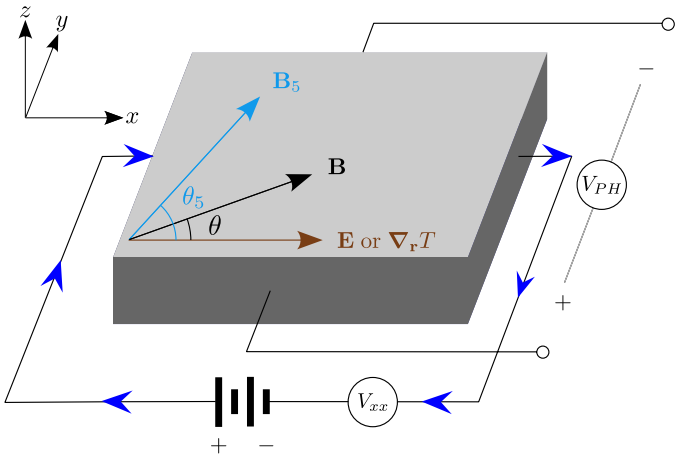

Figure 1. Schematics showing the planar Hall (or planar thermal Hall) experimental set-up, where the sample is subjected to an external electric field $E\,\hat{\mathbf{x}}$ (and/or a temperature gradient $\partial_x T\,\hat{\mathbf{x}}$). An external magnetic field $\mathbf{B}$ is applied such that it makes an angle θ with the existing electric field (and/or the temperature gradient). In addition, the sample is considered to be under the influence of a mechanical strain, whose effect is incorporated via an artificial chiral gauge field $\mathbf{B}_5$, making an angle θ_5 with the x-axis. The resulting planar Hall (or planar thermal Hall) voltage, generated along the y-axis, is indicated by the symbol V_{PH}.

The paper is organized as follows: In Sect. "Model", we describe the low-energy effective Hamiltonians for the WSMs and mWSMs. In Sects. "Magnetoelectric conductivity", "Magnetothermoelectric conductivity", and "Magnetothermal coefficient", we show the explicit expressions of the in-plane components of the response tensors, and discuss their behaviour in some relevant parameter regimes. Finally, we conclude with a summary and outlook in Sect. "Summary and future perspectives". The appendices are devoted to explaining the details of the intermediate steps used to derive the final expressions in the main text.

Model

In the vicinity of a nodal point with chirality χ and Berry monopole charge of magnitude J, the low-energy effective continuum Hamiltonian is given by[3,4,14]

$$\begin{aligned} \mathcal{H}_\chi(\mathbf{k}) &= \mathbf{d}_\chi(\mathbf{k})\cdot\boldsymbol{\sigma}\,, \quad k_\perp = \sqrt{k_x^2+k_y^2}\,, \quad \phi_k = \arctan\!\left(\frac{k_y}{k_x}\right), \quad \alpha_J = \frac{v_\perp}{k_0^{J-1}}\,, \\ \mathbf{d}_\chi(\mathbf{k}) &= \Big\{\alpha_J\, k_\perp^J\cos(J\phi_k),\, \alpha_J\, k_\perp^J\sin(J\phi_k),\, \chi\, v_z\, k_z\Big\}, \end{aligned} \tag{1}$$

where $\boldsymbol{\sigma} = \{\sigma_x, \sigma_y, \sigma_z\}$ is the vector operator consisting of the three Pauli matrices, σ_0 is the 2×2 identity matrix, $\chi \in \{1,-1\}$ denotes the chirality of the node, and v_z ($v_\perp$) is the Fermi velocity along the z-direction (xy-plane). The parameter k_0 has the dimension of momentum, whose value depends on the microscopic details of the material in consideration. The eigenvalues of the Hamiltonian are given by

$$\varepsilon_{\chi,s}(\mathbf{k}) = (-1)^{s+1}\,\epsilon_{\mathbf{k}}\,, \quad s\in\{1,2\}, \quad \epsilon_{\mathbf{k}} = \sqrt{\alpha_J^2\, k_\perp^{2J} + v_z^2\, k_z^2}\,, \tag{2}$$

where the value 1 (2) for s represents the conduction (valence) band [cf. Fig. 2]. We note that we recover the linear and isotropic nature of a WSM by setting $J=1$ and $\alpha_1 = v_z$.

The band velocity of the chiral quasiparticles is given by

$$\boldsymbol{v}^{(0)}_{\chi,s}(\mathbf{k}) \equiv \nabla_{\mathbf{k}}\varepsilon_{\chi,s}(\mathbf{k}) = -\frac{(-1)^s}{\epsilon_{\mathbf{k}}}\Big\{J\,\alpha_J^2\, k_\perp^{2J-2}\, k_x,\, J\,\alpha_J^2\, k_\perp^{2J-2}\, k_y,\, v_z^2\, k_z\Big\}\,. \tag{3}$$

The Berry curvature (BC) and the orbital magnetic moment (OMM), associated with the s^{th} band, are expressed by[51–54]

$$\begin{aligned} \boldsymbol{\Omega}_{\chi,s}(\mathbf{k}) &= i\,\langle\nabla_{\mathbf{k}}\psi_s^\chi(\mathbf{k})|\times|\nabla_{\mathbf{k}}\psi_s^\chi(\mathbf{k})\rangle \Rightarrow \Omega^i_{\chi,s}(\mathbf{k}) = \frac{(-1)^s\,\epsilon^i{}_{jl}}{4\,|\mathbf{d}_\chi(\mathbf{k})|^3}\,\mathbf{d}_\chi(\mathbf{k})\cdot\Big[\partial_{k_j}\mathbf{d}_\chi(\mathbf{k})\times\partial_{k_l}\mathbf{d}_\chi(\mathbf{k})\Big] \\ \text{and } \boldsymbol{m}_{\chi,s}(\mathbf{k}) &= -\frac{i\,e}{2}\,\langle\nabla_{\mathbf{k}}\psi_s(\mathbf{k})|\times\Big[\big\{\mathcal{H}(\mathbf{k})-\mathcal{E}_{\chi,s}(\mathbf{k})\big\}|\nabla_{\mathbf{k}}\psi_s(\mathbf{k})\rangle\Big] \\ \Rightarrow m^i_{\chi,s}(\mathbf{k}) &= \frac{e\,\epsilon^i{}_{jl}}{4\,|\mathbf{d}_\chi(\mathbf{k})|^2}\,\mathbf{d}_\chi(\mathbf{k})\cdot\Big[\partial_{k_j}\mathbf{d}_\chi(\mathbf{k})\times\partial_{k_l}\mathbf{d}_\chi(\mathbf{k})\Big], \end{aligned} \tag{4}$$

respectively, where the indices i, j, and $l\in\{x,y,z\}$, and are used to denote the Cartesian components of the 3d vectors and tensors. The symbol $|\psi_s^\chi(\mathbf{k})\rangle$ denotes the normalized eigenvector corresponding to the band labelled by s, with $\{|\psi_1^\chi\rangle,\ \{|\psi_2^\chi\rangle\}$ forming an orthonormal set for each node.

On evaluating the expressions in Eq. (4), using Eq. (1), we get

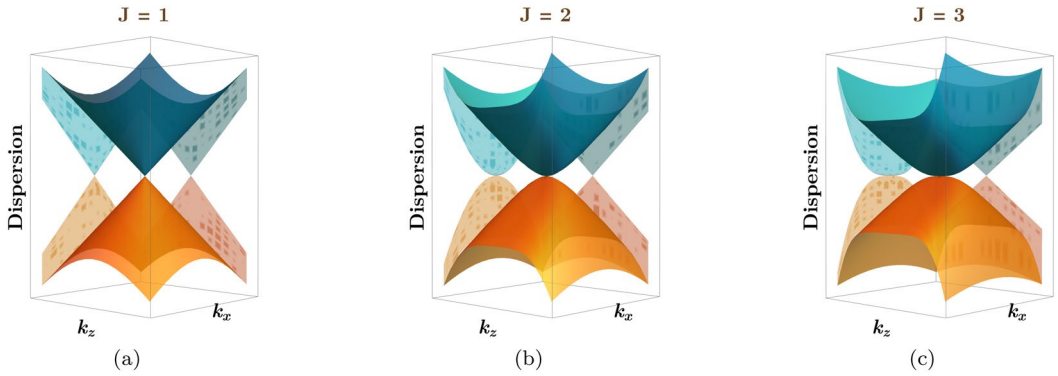

Figure 2. Schematic dispersion of a single node in a (**a**) Weyl, (**b**) double-Weyl, and (**c**) triple-Weyl semimetal, plotted against the k_zk_x-plane. The double(triple)-Weyl node shows an anisotropic hybrid dispersion with a quadratic(cubic)-in-momentum dependence along the k_x-direction. In order to pinpoint the direction-dependent features, the projections of the dispersion along the respective momentum axes are also shown.

$$\boldsymbol{\Omega}_{\chi,s}(\mathbf{k}) = \frac{\chi\,(-1)^s J\, v_z\, \alpha_J^2\, k_\perp^{2J-2}}{2\,\epsilon_{\mathbf{k}}^3}\{k_x,\, k_y,\, J\,k_z\}, \quad \boldsymbol{m}_{\chi,s}(\mathbf{k}) = -\frac{\chi\, e J\, v_z\, \alpha_J^2\, k_\perp^{2J-2}}{2\,\epsilon_{\mathbf{k}}^2}\{k_x,\, k_y,\, J\,k_z\}. \tag{5}$$

From these expressions, we immediately observe the identity

$$\boldsymbol{m}_{\chi,s}(\mathbf{k}) = -(-1)^s\, e\,\epsilon_{\mathbf{k}}\,\boldsymbol{\Omega}_{\chi,s}(\mathbf{k})\,. \tag{6}$$

While the BC changes sign with s, the OMM does not.

In this paper, we will take a positive value of the chemical potential μ, such that it cuts the conduction bands with $s = 1$. Henceforth, we will use the notations $\varepsilon_{\chi,1} = \varepsilon_\chi$, $\boldsymbol{v}^{(0)}_{\chi,1} = \boldsymbol{v}^{(0)}$ (since it is independent of χ), $\Omega_{\chi,1} = \Omega_\chi$, and $\boldsymbol{m}_{\chi,1} = \boldsymbol{m}_\chi$, in order to avoid cluttering. The ranges of the values of the parameters that we will use in our computations are shown in Table 1.

Response tensors using the Boltzmann formalism

Using the semiclassical Boltzmann formalism[57,58], the transport coefficients can be determined in the weak $|\mathbf{B}_\chi|$ limit, which applies to the regime of small cyclotron frequency, implying that the Landau-level quantization can be ignored. The detailed steps can be found in the Appendix A of Ref.38, which we do not repeat here for the sake of brevity. Moreover, we work with the relation-time approximation for the collision integral, taking a simplistic momentum-independent relaxation time τ. Furthermore, we assume that intranode scatterings are dominant over the internode scattering processes, such that τ corresponds only to the former.

Let the contributions to the average electric and thermal current densities from the quasiparticles, associated with the node of chirality χ, be $\mathbf{J}^\chi$ and $\mathbf{J}^{\mathrm{th},\chi}$, respectively. The response matrix, which relates the resulting generalized currents to the driving electric potential gradient and/or temperature gradient, can be expressed as

$$\begin{pmatrix} J_i^\chi \\ J_i^{\mathrm{th},\chi} \end{pmatrix} = \sum_j \begin{pmatrix} \sigma_{ij}^\chi & \alpha_{ij}^\chi \\ T\,\alpha_{ij}^\chi & \ell_{ij}^\chi \end{pmatrix} \begin{pmatrix} E_j \\ -\partial_j T \end{pmatrix}. \tag{7}$$

Here, σ_{ij}^χ and α_{ij}^χ represent the components of the magnetoelectric conductivity tensor (σ^χ) and the magnetothermoelectric conductivity tensor (α^χ), respectively. While α^χ determines the Peltier (Π^χ), Seebeck (S), and Nernst coefficients, ℓ^χ is the linear response tensor relating the heat current density to the temperature gradient, at a vanishing electric field. S^χ, Π^χ, and the magnetothermal conductivity tensor κ^χ (which provides the coefficients between the heat current density and the temperature gradient at vanishing electric current) can be extracted from the coefficients on the right-hand-side of Eq. (7), via the following relations[57,58]:

$$S_{ij}^\chi = \sum_{a'} \left(\sigma^\chi\right)^{-1}_{ii'} \alpha^\chi_{i'j}\,, \quad \Pi_{ij}^\chi = T \sum_{i'} \alpha^\chi_{ii'} \left(\sigma^\chi\right)^{-1}_{i'j}\,, \quad \kappa_{ij}^\chi = \ell_{ij}^\chi - T \sum_{i',j'} \alpha^\chi_{ii'} \left(\sigma^\chi\right)^{-1}_{i'j'} \alpha^\chi_{j'j}\,. \tag{8}$$

In order to include the effects from the OMM and the BC, we first define the quantitites

$$\begin{aligned} \mathcal{E}_\chi(\mathbf{k}) &= \varepsilon_\chi(\mathbf{k}) + \varepsilon_\chi^{(m)}(\mathbf{k})\,, \quad \varepsilon_\chi^{(m)}(\mathbf{k}) = -\,\mathbf{B}_\chi \cdot \mathbf{m}_\chi(\mathbf{k})\,, \\ \boldsymbol{v}_\chi(\mathbf{k}) &\equiv \nabla_{\mathbf{k}} \mathcal{E}_\chi(\mathbf{k}) = \boldsymbol{v}^{(0)}(\mathbf{k}) + \boldsymbol{v}_\chi^{(m)}(\mathbf{k})\,, \\ \boldsymbol{v}_\chi^{(m)}(\mathbf{k}) &= \nabla_{\mathbf{k}} \varepsilon_\chi^{(m)}(\mathbf{k})\,, \quad D_\chi = \left[1 + e\left\{\mathbf{B}_\chi \cdot \boldsymbol{\Omega}_\chi(\mathbf{k})\right\}\right]^{-1}, \end{aligned} \tag{9}$$

where $\varepsilon_\chi^{(m)}(\mathbf{k})$ is the Zeeman-like correction to the energy due to the OMM, $\boldsymbol{v}_\chi(\mathbf{k})$ is the modified band velocity of the Bloch electrons after including $\varepsilon_\chi^{(m)}(\mathbf{k})$, and D_χ is the modification factor of the phase space volume element due to a nonzero BC. The modification of the effective Fermi surface, on including the correction $\varepsilon_\chi^{(m)}(\mathbf{k})$, is shown schematically in Fig. 3.

Our weak-magnetic-field limit implies that

$$e\,\mathbf{B}_\chi \cdot \boldsymbol{\Omega}_\chi \ll 1. \tag{10}$$

Parameter	SI units	Natural units
v_z from Ref.55	15×10^5 m s^{-1}	0.005
τ from Ref.56	10^{-13} s	152 eV^{-1}
T from Ref.20	$10 - 100$ K	$8.617 \times 10^{-4} - 8.617 \times 10^{-3}$ eV
B and B_5 from Ref.48	$0 - 10$ Tesla	$0 - 2000$ eV^2
μ from Refs.20,55	$1.6 \times 10^{-21} - 1.6 \times 10^{-20}$ J	$0.01 - 0.1$ eV

Table 1. The values of the various parameters which we have used in plotting the transport coefficients are tabulated here. Since $\alpha_J = v_\perp / k_0^{J-1}$, we get $\alpha_1 = v_z$, $\alpha_2 = v_\perp/k_0$, and $\alpha_3 = v_\perp/k_0^2 = \alpha_2^2/\alpha_1$. In terms of natural units, we need to set $\hbar = c = k_B = 1$, and $4\,\pi\,\epsilon_0 = 137$. In our plots, we have used $v_\perp = v_z$ (from the table entry), leading to $\alpha_2 = 3.9 \times 10^{-5}$ eV^{-1} and $\alpha_3 = 2.298 \times 10^{-6}$ eV^{-2}. For $J = 2$ and $J = 3$, $v_\perp$ has been set equal to v_z for the sake of simplicity, while the isotropic dispersion for $J = 1$ has $v_\perp = v_z$ automatically.

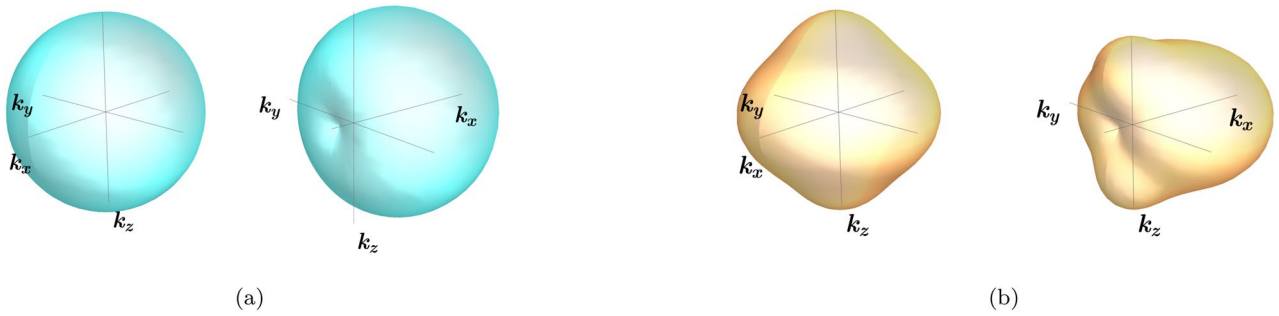

(a) (b)

Figure 3. Schematics of the Fermi surfaces for one node of a (**a**) WSM and (**b**) double-Weyl semimetal, without and with the OMM-correction for the effective energy dispersion. Here we have taken the effective magnetic field to be directed purely along the x-axis.

In our calculations, we keep terms upto $\mathcal{O}(|\mathbf{B}_\chi|^2)$ and, thus, use

$$D_\chi = 1 - e\left(\mathbf{B}_\chi \cdot \mathbf{\Omega}_\chi\right) + e^2\left(\mathbf{B}_\chi \cdot \mathbf{\Omega}_\chi\right)^2 + \mathcal{O}(|\mathbf{B}_\chi|^3)\,. \tag{11}$$

Also, the condition in Eq. (10) implies that $|\varepsilon_\chi^{(m)}(\mathbf{k})|$ is small compared to $\varepsilon_\chi(\mathbf{k})$:

$$|\mathbf{B}_\chi \cdot \boldsymbol{m}_\chi| = \varepsilon_\chi\, e\big(\mathbf{B}_\chi \cdot \mathbf{\Omega}_\chi\big) \ll \varepsilon_\chi\,. \tag{12}$$

This means that the Fermi-Dirac distribution can also be power expanded up to quadratic order in the magnetic field, as follows:

$$f_0(\mathcal{E}_\chi) = f_0(\varepsilon_\chi) + \varepsilon_\chi^{(m)} f_0'(\varepsilon_\chi) + \frac{1}{2}\left(\varepsilon_\chi^m\right)^2 f_0''(\varepsilon_\chi) + \mathcal{O}(|\mathbf{B}_\chi|^3)\,, \tag{13}$$

where the prime indicates derivative with respect to the energy argument of f_0.

The general expression for the magnetoelectric conductivity tensor for an isolated node of chirality χ, contributed by the conduction band, is given by

$$\sigma_{ij}^{\chi} = -e^2\,\tau \int \frac{d^3\mathbf{k}}{(2\pi)^3}\, D_\chi \left[v_{\chi i} + e\,(\boldsymbol{v}_\chi \cdot \mathbf{\Omega}_\chi)\, B_{\chi i}\right]\left[v_{\chi j} + e\,(\boldsymbol{v}_\chi \cdot \mathbf{\Omega}_\chi)\, B_{\chi j}\right] \frac{\partial f_0(\mathcal{E}_\chi)}{\partial \mathcal{E}_\chi}, \tag{14}$$

where we do not include the parts coming from the "intrinsic anomalous Hall" effect and the so-called Lorentz-force contribution. This is because of the following reasons:

1. The intrinsic anomalous Hall term is given by

$$\begin{aligned}
\sigma_{ij}^{\mathrm{AH},\chi} &= -e^2\,\epsilon_{ijl}\int \frac{d^3\mathbf{k}}{(2\pi)^3}\,\Omega_\chi^l(\mathbf{k})\, f_0(\mathcal{E}_\chi) = \sigma_{ij}^{\mathrm{AH(0)},\chi} + \sigma_{ij}^{\mathrm{AH(1)},\chi} + \sigma_{ij}^{\mathrm{AH(2)},\chi} + \mathcal{O}(|\mathbf{B}_\chi|^3)\,,\\
\sigma_{ij}^{\mathrm{AH(0)},\chi} &= -e^2\,\epsilon_{ijl}\int \frac{d^3\mathbf{k}}{(2\pi)^3}\,\Omega_\chi^l(\mathbf{k})\, f_0(\varepsilon_\chi)\,, \quad \sigma_{ij}^{\mathrm{AH(1)},\chi} = -e^2\,\epsilon_{ijl}\int \frac{d^3\mathbf{k}}{(2\pi)^3}\,\Omega_\chi^l(\mathbf{k})\,\varepsilon_\chi^{(m)} f_0'(\varepsilon_\chi)\,,\\
\sigma_{ij}^{\mathrm{AH(2)},\chi} &= -\frac{e^2\,\epsilon_{ijl}}{2}\int \frac{d^3\mathbf{k}}{(2\pi)^3}\,\Omega_\chi^l(\mathbf{k})\left(\varepsilon_\chi^m\right)^2 f_0''(\varepsilon_\chi)\,,
\end{aligned} \tag{15}$$

whose diagonal components (i.e., $\sigma_{ii}^{\mathrm{AH},\chi}$) are automatically zero. The first term, $\sigma_{ij}^{\mathrm{AH(0)},\chi}$, is $\mathbf{B}_\chi$-independent and vanishes identically. The nonzero OMM generates $\mathbf{B}_\chi$-dependent terms. However, for our configuration consisting of $\mathbf{E}$- and $\mathbf{B}_\chi$-components lying in the xy-plane, we have

$$\begin{aligned}
&\sigma_{yx}^{\mathrm{AH}\,(1),\chi} = \sigma_{xy}^{\mathrm{AH}\,(1),\chi}\\
&\propto \int_{-\infty}^{\infty} k_z\, dk_z \int_0^{\infty} dk_\perp\, \frac{k_\perp^{4J-2}}{\varepsilon_\chi^5} f_0'(\varepsilon_\chi) \int_0^{2\pi} d\phi \left[B_{\chi x}\cos\phi + B_{\chi y}\sin\phi\right] = 0\,,\\
&\text{and } \sigma_{yx}^{\mathrm{AH}\,(2),\chi} = \sigma_{yx}^{\mathrm{AH}\,(2),\chi} = 0\,.
\end{aligned} \tag{16}$$

Only the transverse out-of-plane components are nonzero, viz.

$$\sigma_{zx}^{\mathrm{AH}\,(1),\chi}(\mu_\chi) = \frac{e^3\,J\,v_z\,B_{\chi y}}{24\,\pi^2}\int_0^\infty d\varepsilon_\chi\,\frac{f_0'(\varepsilon_\chi)}{\varepsilon_\chi} = -\frac{e^3\,J\,v_z\,B_{\chi y}}{24\,\pi^2\,\mu_\chi}\left(1+\frac{\pi^2}{3\,\beta^2\,\mu_\chi^2}\right) \text{ and}$$
$$\sigma_{zy}^{\mathrm{AH}\,(1),\chi}(\mu_\chi) = \frac{e^3\,J\,v_z\,B_{\chi x}}{24\,\pi^2\,\mu_\chi}\left(1+\frac{\pi^2}{3\,\beta^2\,\mu_\chi^2}\right) \text{ [if we have a nonzero } y\text{-component of } \mathbf{E}\text{]}. \tag{17}$$

We note that $\sigma_{zx}^{\mathrm{AH}\,(2),\chi} = \sigma_{zy}^{\mathrm{AH}\,(2),\chi} = 0$. Since we are focussing on the in-plane components of the response tensors, we will not discuss further the behaviour of these nonzero out-of-plane components.

2. The Lorentz-force part shows a behaviour analogous to the intrinsic anomalous Hall part described above, with vanishing in-plane components (see Ref.40 for generic arguments stemming from symmetry considerations).

The expression for σ_{ij}^{χ}, shown above, includes the effects of the BC and the OMM. Here, f_0 is the equilibrium Fermi-Dirac distribution at temperature $T = 1/\beta$ and chemical potential μ_χ. As discussed in Refs.[37,38], while a purely physical magnetic field $\mathbf{B}$ gives a quadratic-dependence of the response on the overall magnetic field, inclusion of a nonzero axial part $\mathbf{B}_5$ opens up the possibility of generating linear and parabolic behaviour of the response tensors.

Analogous to Eq. (14), we have the general expressions[24]

$$\alpha_{ij}^{\chi} = e\,\tau\int\frac{d^3\mathbf{k}}{(2\,\pi)^3}\,D_\chi\left[v_{\chi i}+e\,(\boldsymbol{v}_\chi\cdot\boldsymbol{\Omega}_\chi)\,B_{\chi i}\right]\left[v_{\chi j}+e\,(\boldsymbol{v}_\chi\cdot\boldsymbol{\Omega}_\chi)\,B_{\chi j}\right]\frac{\mathcal{E}_\chi-\mu}{T}\,\frac{\partial f_0(\mathcal{E}_\chi)}{\partial\mathcal{E}_\chi}, \tag{18}$$

and

$$\ell_{ij}^{\chi} = -\,\tau\int\frac{d^3\mathbf{k}}{(2\,\pi)^3}\,D_\chi\left[v_{\chi i}+e\,(\boldsymbol{v}_\chi\cdot\boldsymbol{\Omega}_\chi)\,B_{\chi i}\right]\left[v_{\chi j}+e\,(\boldsymbol{v}_\chi\cdot\boldsymbol{\Omega}_\chi)\,B_{\chi j}\right]\frac{(\mathcal{E}_\chi-\mu)^2}{T}\,\frac{\partial f_0(\mathcal{E}_\chi)}{\partial\mathcal{E}_\chi}, \tag{19}$$

respectively. Since ℓ^χ determines the first term in the magnetothermal conductivity tensor κ^χ, we will often loosely refer to ℓ^χ itself as the magnetothermal coefficient.

Magnetoelectric conductivity

Working in the weak-in-magnetic-field limit, which allows expansions in the components of $\mathbf{B}_\chi$, the terms in Eq. (14) are disentangled into a sum of three terms, having distinct origins, as follows:

$$\sigma_{ij}^{\chi} = \sigma_{ij}^{0,\chi} + \sigma_{ij}^{\Omega,\chi} + \sigma_{ij}^{m,\chi}\,. \tag{20}$$

Here,

$$\sigma_{ij}^{0,\chi} = -e^2\,\tau\int\frac{d^3\mathbf{k}}{(2\,\pi)^3}\,v_{\chi i}^{(0)}\,v_{\chi j}^{(0)}\,f_0'(\varepsilon_\chi), \tag{21}$$

is the conductivity surviving in the absence of a magnetic field (i.e., for $\mathbf{B}_\chi = \mathbf{0}$),

$$\sigma_{ij}^{\Omega,\chi} = -e^4\,\tau\int\frac{d^3\mathbf{k}}{(2\,\pi)^3}\,Q_{\chi i}\,Q_{\chi j}f_0'(\varepsilon_\chi), \quad \mathbf{Q}_\chi = \boldsymbol{\Omega}_\chi\times\left(\boldsymbol{v}_\chi^{(0)}\times\mathbf{B}_\chi\right), \tag{22}$$

is the contribution arising solely from the BC, and

$$\sigma_{ij}^{m,\chi} = 2\,e^3\,\tau\int\frac{d^3\mathbf{k}}{(2\,\pi)^3}\left[Q_{\chi i}\,v_{\chi j}^{(m)}+\frac{\varepsilon_\chi^{(m)}}{e}\left(\nabla_{\mathbf{k}}\cdot\boldsymbol{T}_{\chi ij}\right)+\frac{\varepsilon_\chi^{(m)}}{2}\left(\mathbf{B}_\chi\cdot\boldsymbol{V}_{\chi ij}\right)\frac{\partial}{\partial\varepsilon_\chi}\right]f_0'(\varepsilon_\chi)\,, \tag{23}$$

$$\text{where } \boldsymbol{T}_{\chi ij} = e\,\boldsymbol{\Omega}_\chi\,B_{\chi i}\,v_{\chi j}^{(0)}+\frac{1}{2}\,\hat{\mathbf{e}}_i\,v_{\chi j}^{(m)} \text{ and } \boldsymbol{V}_{\chi ij} = \boldsymbol{\Omega}_\chi\,v_{\chi i}^{(0)}\,v_{\chi j}^{(0)}-\frac{\boldsymbol{m}_\chi}{2\,e}\,\partial_{k^i}\,v_{\chi j}^{(0)}\,, \tag{24}$$

represents the contribution which goes to zero if OMM is set to zero. The symbol $\hat{\mathbf{e}}_i$ represents the unit vector along the Cartesian coordinate axis labelled by i.

The longitudinal and transverse components of the magnetoelectric conductivity tensor σ^χ (i.e., the LMC and the PHC) are computed from the starting expression shown in Eq. (14). The details of the intermediate steps are given in Appendices B and C. Before delving into the investigation of the behaviour of these response coefficients in the subsequent subsections, first let us analyze the relation between the current and the axial electromagnetic fields.

For the quasiparticles with chirality χ, we have the electric current contribution

$$J_i^{\chi}(\mu) = \sigma_{ij}^{\chi}(\mu)\,E_{\chi j}\,, \tag{25}$$

where σ_{ij}^{χ} is given by Eq. (14). For two conjugate nodes with chemical potential values μ_+ and μ_- (as shown schematically in Fig. 4 for WSMs), we define the total and axial currents as

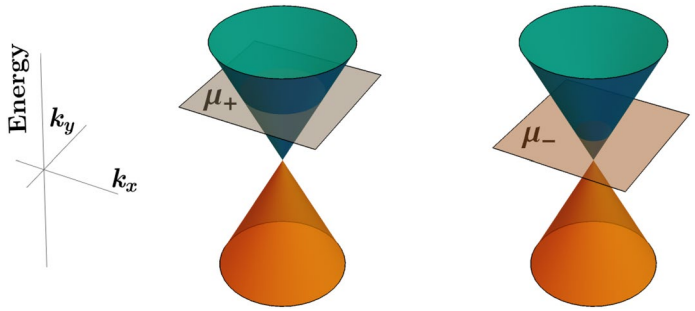

Figure 4. A pair of conjugate Weyl nodes with the corresponding chemical potentials tuned to two different values, μ_+ and μ_-.

$$\begin{aligned} \boldsymbol{J}(\mu_+,\mu_-) &= \sum_{\chi=\pm1} \boldsymbol{J}^{\chi}(\mu_\chi) = \boldsymbol{J}^{+}(\mu_+) + \boldsymbol{J}^{-}(\mu_-) \\ \text{and } \boldsymbol{J}_5(\mu_+,\mu_-) &= \sum_{\chi=\pm1} \chi\, \boldsymbol{J}^{\chi}(\mu_\chi) = \boldsymbol{J}^{+}(\mu_+) - \boldsymbol{J}^{-}(\mu_+)\,, \end{aligned} \tag{26}$$

respectively. These suggest to introduce analogous expressions for the conductivity tensors as

$$\sigma_{ij}(\mu_+,\mu_-) = \sum_{\chi=\pm1} \sigma_{ij}^{\chi}(\mu_\chi) \text{ and } \sigma_{5ij} = \sum_{\chi=\pm1} \chi\, \sigma_{ij}^{\chi}(\mu_\chi)\,. \tag{27}$$

Using Eq. (27), we find that

$$\begin{aligned} J_i(\mu_+,\mu_-) &= \sigma_{ij}^{+}(\mu_+)\, E_{+j} + \sigma_{ij}^{-}(\mu_-)\, E_{-j} = \sigma_{ij}(\mu_+,\mu_-)\, E_j + \sigma_{5ij}(\mu_+,\mu_-)\, E_{5j} \\ \text{and } J_{5i}(\mu_+,\mu_-) &= \sigma_{ij}^{+}(\mu_+)\, E_{+j} - \sigma_{ij}^{-}(\mu_-)\, E_{-j} = \sigma_{5ij}(\mu_+,\mu_-)\, E_j + \sigma_{ij}(\mu_+,\mu_-)\, E_{5j}\,, \end{aligned} \tag{28}$$

where $\mathbf{E}_5$ is an axial pseudoelectric field, which can be generated artificially (as explained in the introduction). For the node with chirality χ, analogous to $\mathbf{B}_\chi$, the physical $\mathbf{E}$ and the axial $\mathbf{E}_5$ add up to give the effective electric field $\mathbf{E}_\chi = \mathbf{E} + \chi\, \mathbf{E}_5$, reflecting the dependence on χ. In this paper, we deal with the case where $\mathbf{E}_5 = \mathbf{0}$.

From the above expressions for the total and axial currents, we now discuss the behaviour of the total and axial LMC and PHC as functions of θ, which is the angle between $\mathbf{E}$ and $\mathbf{B}$, with the former chosen to be directed along the x-axis [cf. Fig. 1]. For the illustration of the behaviour of the response, we define

$$\begin{aligned} \Sigma_{ij}(\mathbf{B}_\chi) &= \sigma_{ij}(\mu_+,\mu_-) - \sigma_{ij}(\mu_+,\mu_-)\Big|_{\mathbf{B}_\chi=\mathbf{0}} \\ \text{and } \Sigma_{5ij}(\mathbf{B}_\chi) &= \sigma_{5ij}(\mu_+,\mu_-) - \sigma_{5ij}(\mu_+,\mu_-)\Big|_{\mathbf{B}_\chi=\mathbf{0}} \end{aligned} \tag{29}$$

for the total and axial conductivity tensor components, respectively, after subtracting off the $\mathbf{B}_\chi$-independent parts. We denote the parts connected with $\sigma_{ij}^{\Omega,\chi}$ and $\sigma_{ij}^{m,\chi}$ as $(\Sigma_{ij}^{\Omega},\ \Sigma_{5ij}^{\Omega})$ and $(\Sigma_{ij}^{m},\ \Sigma_{5ij}^{m})$, respectively. Therefore, if the OMM is not considered, each of $(\Sigma_{ij}^{m},\ \Sigma_{5ij}^{m})$ goes to zero.

Longitudinal magnetoconductivity

Using the explicit expressions derived in Appendix B, we have

$$\sigma_{xx}^{\chi}(\mu_\chi) = \sigma_{xx}^{0,\chi}(\mu_\chi) + \sigma_{xx}^{\Omega,\chi}(\mu_\chi) + \sigma_{xx}^{m,\chi}(\mu_\chi)\,, \tag{30}$$

where

$$\begin{aligned} \sigma_{xx}^{0,\chi}(\mu_\chi) &= \frac{e^2\,\tau\,J}{6\,\pi^2\,v_z}\,\Lambda_2(\mu_\chi)\,, \\ \sigma_{xx}^{\Omega,\chi}(\mu_\chi) &= \frac{e^4\,\tau\,v_z\,\alpha_J^{\frac{2}{J}}\,\Lambda_{-\frac{2}{J}}(\mu_\chi)}{128\,\pi^{\frac{3}{2}}}\,\frac{\Gamma\left(2-\frac{1}{J}\right)}{\Gamma\left(\frac{9}{2}-\frac{1}{J}\right)}\left[g_x^{bc}(J)\,B_{\chi x}^2 + g_y^{bc}(J)\,B_{\chi y}^2\right], \\ \sigma_{xx}^{m,\chi}(\mu_\chi) &= \frac{e^4\,\tau\,v_z\,\alpha_J^{\frac{2}{J}}\,\Lambda_{-\frac{2}{J}}(\mu_\chi)\,\Gamma\left(2-\frac{1}{J}\right)}{128\,\pi^{\frac{3}{2}}\,\Gamma\left(\frac{9}{2}-\frac{1}{J}\right)}\left[g_x^{m}(J)\,B_{\chi x}^2 + g_y^{m}(J)\,B_{\chi y}^2\right], \end{aligned} \tag{31}$$

and

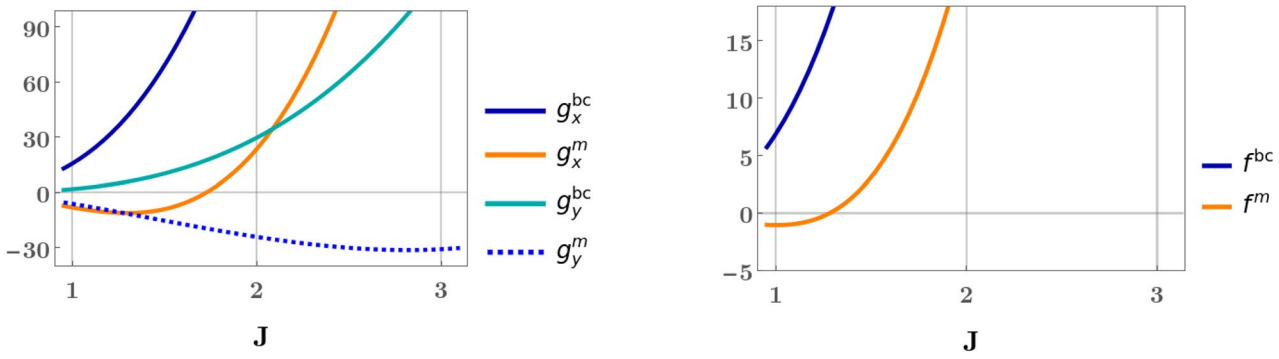

Figure 5. Comparison of the values of the functions defined in Eqs. (32) and (35) for $J = 1,\ 2,\ 3$.

$$g_x^{bc}(J) = J\left(32J^2 - 19J + 3\right), \quad g_y^{bc}(J) = J(3J-1)(2J-1),$$
$$g_x^{m}(J) = \frac{37J^4 - 100J^3 + 74J^2 - 21J + 2}{J}, \quad g_y^{m}(J) = \frac{3J^4 - 12J^3 - 4J^2 + 9J - 2}{J}. \tag{32}$$

From Fig. 5, we find that (1) $g_x^{bc}(J)$ and $g_y^{bc}(J)$ are positive for all J-values; (2) $g_x^{m}(J)$ is negative for $J = 1$ and positive for $J = 2,\ 3$; (3) $g_y^{m}(J)$ is negative for all J-values. For $J = 1$, the OMM acts in opposition to the BC-only term for the $B_{\chi x}$-part, and reduces the overall response. On the other hand, for the mWSMs, the OMM adds up to the BC-only term for the $B_{\chi x}$-part, thus increasing the overall response. For the $B_{\chi y}$-part, the OMM and the BC-only parts always have opposite signs and, thus, tend to reduce the overall response's magnitude. Therefore, for a WSM, the OMM part always reduces the value of σ_{xx}^{χ} by adding a negative contribution.

In order to estimate the effects of the OMM (which was neglected in many earlier works), we plot the behaviour of Σ_{xx}^{Ω}, Σ_{xx}^{m}, Σ_{5xx}^{Ω}, and Σ_{5xx}^{m} in Figs. 6 and 7. The interplay of the BC-only and the OMM-induced parts are illustrated via some representative parameter values. In agreement with our comparison of the g-values, we find that for a WSM, the OMM can even change the sign of the response, depending on the net magnetic field. However, for $J = 2,\ 3$, the g_x^m and the g_y^m-parts have opposite signs — hence, their combined effects may increase or reduce the overall response. From Fig. 6, we find that, turning on a nonzero $\mathbf{B}_5$-part changes the periodicity, with respect to θ, from π to 2π. This is completely expected because the axial pseudomagnetic field causes linear-in-$B\cos\theta$ and/or linear-in-$B\sin\theta$ terms to appear, in addition to the quadratic-in-B_i dependence of the untilted WSMs/mWSMs.

Planar Hall conductivity

Using the explicit expressions derived in Appendix C, we have

$$\sigma_{yx}^{\chi}(\mu_\chi) = \sigma_{xy}^{\chi}(\mu_\chi) = \sigma_{xy}^{0,\chi}(\mu_\chi) + \sigma_{xy}^{\Omega,\chi}(\mu_\chi) + \sigma_{xy}^{m,\chi}(\mu_\chi), \tag{33}$$

where

$$\sigma_{xy}^{0,\chi}(\mu_\chi) = 0, \quad \sigma_{xy}^{\Omega,\chi}(\mu_\chi) = \frac{e^4\,\tau\,v_z\,\alpha_J^{\frac{2}{J}}\,\Lambda_{-\frac{2}{J}}(\mu_\chi)}{64\,\pi^{\frac{3}{2}}}\,\frac{\Gamma\left(2-\frac{1}{J}\right)}{\Gamma\left(\frac{9}{2}-\frac{1}{J}\right)}\,f^{bc}(J)\,B_{\chi x}\,B_{\chi y},$$
$$\sigma_{xy}^{m,\chi}(\mu_\chi) = \frac{e^4\,\tau\,v_z\,\alpha_J^{\frac{2}{J}}\,\Lambda_{-\frac{2}{J}}(\mu_\chi)}{64\,\pi^{\frac{3}{2}}}\,\frac{\Gamma\left(2-\frac{1}{J}\right)}{\Gamma\left(\frac{9}{2}-\frac{1}{J}\right)}\,f^{m}(J)\,B_{\chi x}\,B_{\chi y}, \tag{34}$$

and

$$f^{bc}(J) = J\left(13J^2 - 7J + 1\right), \quad f^{m}(J) = 17J^3 - 44J^2 + 39J - 15 + \frac{2}{J}. \tag{35}$$

From Fig. 5, we find that (1) $f^{bc}(J)$ is positive for all J-values; (2) $f^{m}(J)$ is negative for $J = 1$ and positive for $J = 2,\ 3$. For $J = 1$, the OMM thus acts in opposition to the BC-only term, and reduces the magnitude of the overall PHC. In contrast, for the mWSMs, the OMM adds up to the BC-only term, thus increasing the overall response.

In order to estimate the effects of the OMM, we plot the behaviour of Σ_{xy}^{Ω}, Σ_{xy}^{m}, Σ_{5xy}^{Ω}, and Σ_{5xy}^{m} in Figs. 8 and 9. The interplay of the BC-only and the OMM-induced parts are illustrated via the same parameter values as considered for the LMC. In agreement with our comparison of the f-values, we find that for a WSM, the OMM always reduces the response. On the other hand, for $J = 2,\ 3$, the effect of OMM is to enhance the overall response. Analogous to the LMC, Fig. 8 shows that a nonzero $\mathbf{B}_5$-part changes the periodicity with respect to θ

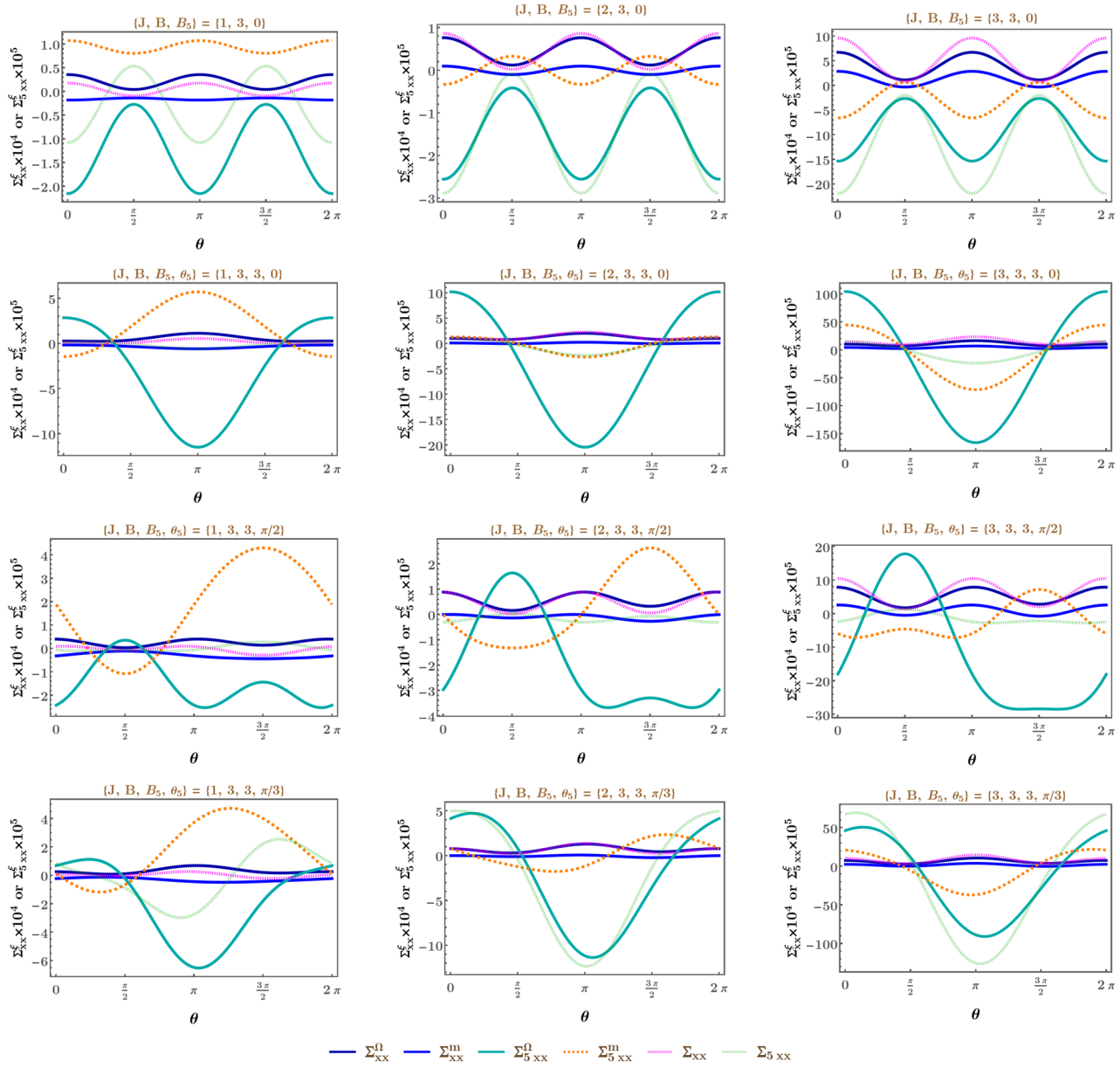

Figure 6. The total and axial combinations of the LMC (in units of eV) for the two conjugate nodes, defined in Eq. (29), as functions of θ, using various values of B (in units of eV^2), B_5 (in units of eV^2), and θ_5 (as indicated in the plotlabels). We have set $v_z = 0.005$, $\tau = 151\,\text{eV}^{-1}$, $\beta = 1160\,\text{eV}^{-1}$, $\mu_+ = 0.4$ eV, and $\mu_- = 0.2$ eV. As explained below Eq. (29), while Σ^{Ω}_{xx} (Σ^{Ω}_{5xx}) represents the part of Σ_{xx} (Σ_{5xx}) originating purely from the BC-contributions (i.e., with no OMM), Σ^{m}_{xx} (Σ^{m}_{5xx}) is the contribution which vanishes if the OMM is not at all considered. We have used the superscript ξ to indicate that, along the vertical axis, we have plotted the BC-only, OMM, and total parts, with the colour-coding shown in the plotlegends. The values of the maxima and minima of the curves are strongly dependent on the values of J.

from π to 2π, which results from the emergence of terms linearly proportional to the components of $\mathbf{B}$, rather than just the quadratic ones.

Magnetothermoelectric conductivity

Defining

$$F^{\chi}_{ij} = D_{\chi}\left[v_{\chi i} + e\,(\boldsymbol{v}_{\chi}\cdot\boldsymbol{\Omega}_{\chi})\,B_{\chi i}\right]\left[v_{\chi j} + e\,(\boldsymbol{v}_{\chi}\cdot\boldsymbol{\Omega}_{\chi})\,B_{\chi j}\right], \tag{36}$$

we expand it as

$$F^{\chi}_{ij} = F^{0,\chi}_{ij} + F^{1,\Omega,\chi}_{ij} + F^{1,m,\chi}_{ij} + F^{2,\Omega,\chi}_{ij} + F^{2,m,\chi}_{ij} + F^{2,(\Omega,m),\chi}_{ij} + \mathcal{O}(|\mathbf{B}_{\chi}|^3)\,, \tag{37}$$

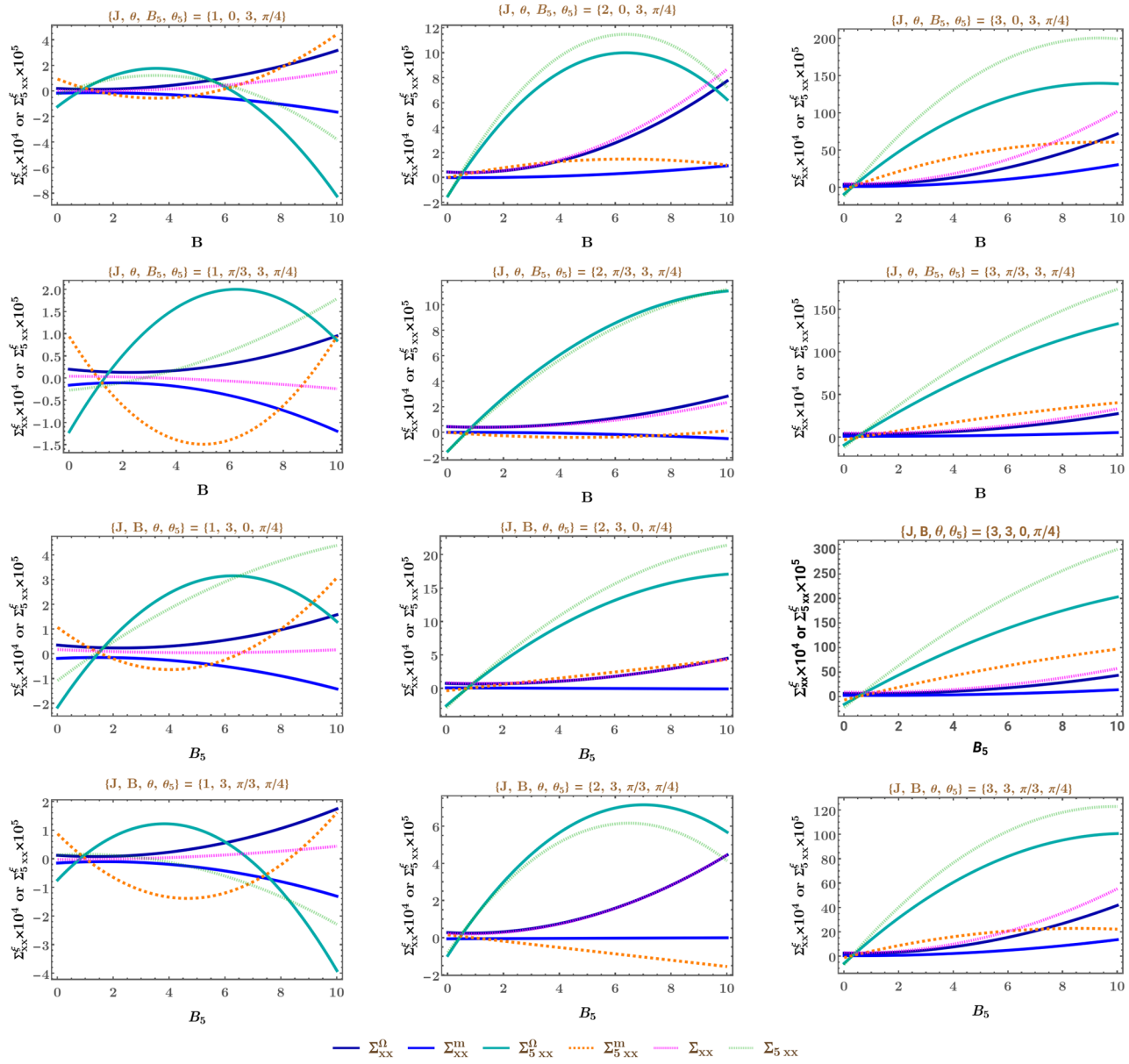

Figure 7. The total and axial combinations of the LMC (in units of eV) for the two conjugate nodes, defined in Eq. (29), as functions of B (in units of eV^2) and B_5 (in units of eV^2), using various values of θ and θ_5 (as indicated in the plotlabels). We have set $\nu_z = 0.005$, $\tau = 151\,\mathrm{eV}^{-1}$, $\beta = 1160\,\mathrm{eV}^{-1}$, $\mu_+ = 0.4$ eV, and $\mu_- = 0.2$ eV. As explained below Eq. (29), while Σ^{Ω}_{xx} (Σ^{Ω}_{5xx}) represents the part of Σ_{xx} (Σ_{5xx}) originating purely from the BC-contributions (i.e., with no OMM), Σ^{m}_{xx} (Σ^{m}_{5xx}) is the contribution which vanishes if the OMM is neglected. We have used the superscript ξ to indicate that, along the vertical axis, we have plotted the BC-only, OMM, and total parts, with the colour-coding shown in the plotlegends.

where

$$
\begin{aligned}
F^{0,\chi}_{ij} &= v^{(0)}_{\chi i}\, v^{(0)}_{\chi j}\,,\\
F^{1,\Omega,\chi}_{ij} &= e\Big[\boldsymbol{v}^{(0)}_{\chi}\cdot\boldsymbol{\Omega}_{\chi}\Big]\Big[v^{(0)}_{\chi i}\,B_{\chi j}+B_{\chi i}\,v^{(0)}_{\chi j}\Big]-e\big(\mathbf{B}_{\chi}\cdot\boldsymbol{\Omega}_{\chi}\big)v^{(0)}_{\chi i}\,v^{(0)}_{\chi j}\,,\\
F^{1,m,\chi}_{ij} &= \Big[v^{(0)}_{\chi i}\,v^{(m)}_{\chi j}+v^{(m)}_{\chi i}\,v^{(0)}_{\chi j}\Big],\\
F^{2,\Omega,\chi}_{ij} &= e^2\,Q_{\chi i}\,Q_{\chi j}\,,\quad F^{2,m,\chi}_{ij} = v^{(m)}_{\chi i}\,v^{(m)}_{\chi j}\,,\\
F^{2,(\Omega,m),\chi}_{ij} &= e\Big[\boldsymbol{v}^{(0)}_{\chi}\cdot\boldsymbol{\Omega}_{\chi}\Big]\Big[v^{(m)}_{\chi i}\,B_{\chi j}+B_{\chi i}\,v^{(m)}_{\chi j}\Big]+e\Big[\boldsymbol{v}^{(m)}_{\chi}\cdot\boldsymbol{\Omega}_{\chi}\Big]\Big[v^{(0)}_{\chi i}\,B_{\chi j}+B_{\chi i}\,v^{(0)}_{\chi j}\Big]\\
&\quad -e\big(\mathbf{B}_{\chi}\cdot\boldsymbol{\Omega}_{\chi}\big)\Big[v^{(0)}_{\chi i}\,v^{(m)}_{\chi j}+v^{(m)}_{\chi i}\,v^{(0)}_{\chi j}\Big].
\end{aligned}
\tag{38}
$$

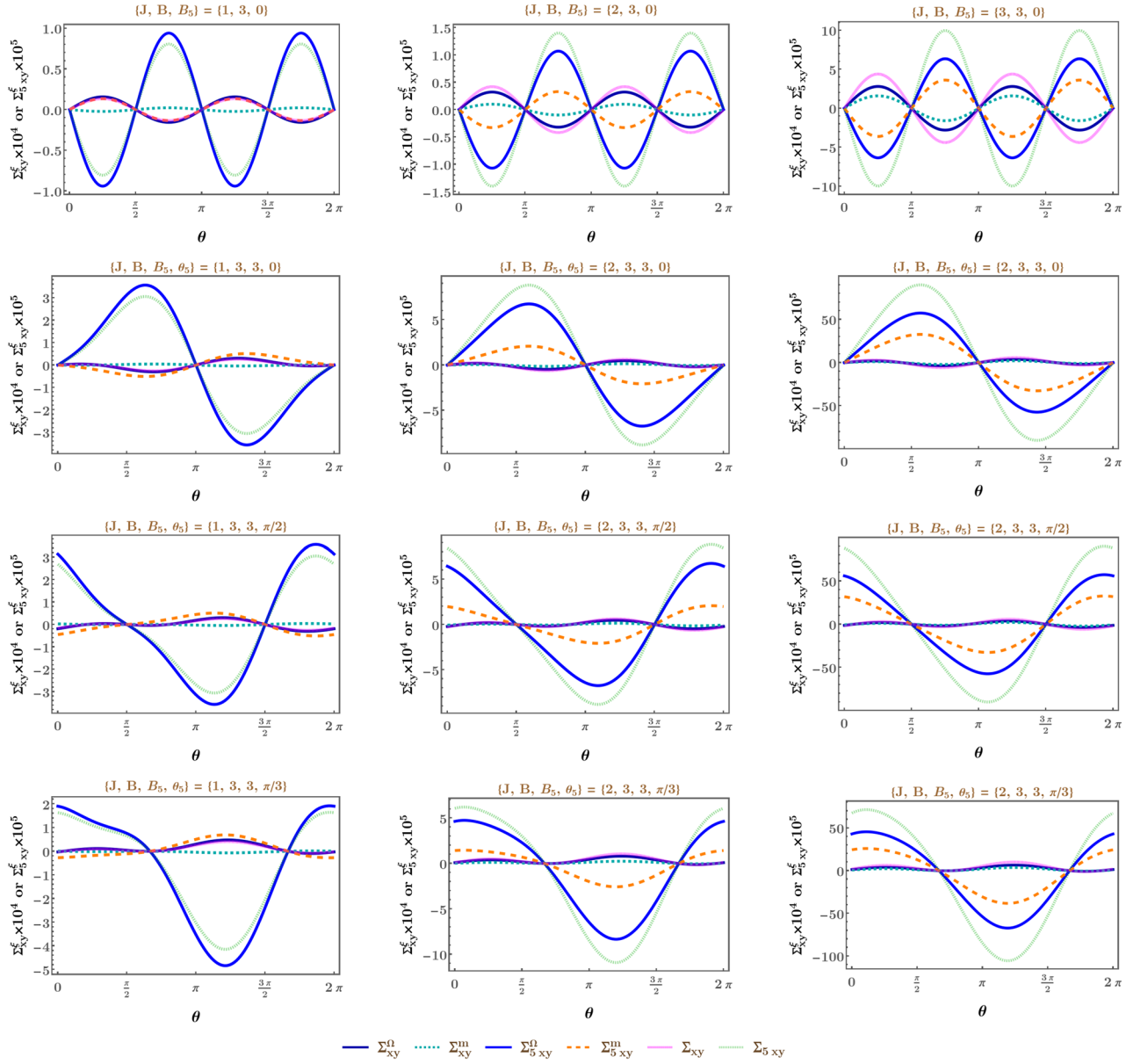

Figure 8. The total and axial combinations of the PHC (in units of eV) for the two conjugate nodes, defined in Eq. (29), as functions of θ, using various values of B (in units of eV^2), B_5 (in units of eV^2), and θ_5 (as indicated in the plotlabels). We have set $v_z = 0.005$, $\tau = 151\,\text{eV}^{-1}$, $\beta = 1160\,\text{eV}^{-1}$, $\mu_+ = 0.4$ eV, and $\mu_- = 0.2$ eV. As explained below Eq. (29), while Σ^{Ω}_{xy} (Σ^{Ω}_{5xy}) represents the part of Σ_{xy} (Σ_{5xy}) originating purely from the BC-contributions (i.e., with no OMM), Σ^{m}_{xy} (Σ^{m}_{5xy}) is the contribution which vanishes if the OMM is not at all considered. We have used the superscript ξ to indicate that, along the vertical axis, we have plotted the BC-only, OMM, and (BC + OMM) parts, with the colour-coding shown in the plotlegends. The values of the maxima and minima of the curves are strongly dependent on the values of J.

Here, $F^{0,\chi}_{ij}$ is $\mathbf{B}_\chi$-independent, $F^{1,\Omega,\chi}_{ij}$ is linear in the components of the BC, $F^{1,m,\chi}_{ij}$ is linear in the OMM-contributions, $F^{2,\Omega,\chi}_{ij}$ is quadratic in the components of the BC, $F^{1,m,\chi}_{ij}$ is quadratic in the OMM-contributions, and $F^{2,(\Omega,m),\chi}_{ij}$ is a mixed term which contains products of the BC-components and the OMM-contributions.

Using the above expressions for the function defined as $G^{\chi}_{ij} = F^{\chi}_{ij}\,\frac{\mathcal{E}_\chi - \mu}{T}$, the weak-field expansion gives us

$$\begin{aligned} G^{\chi}_{ij} &= F^{\chi}_{ij}\,\frac{\varepsilon_\chi - \mu}{T} + \left[F^{0,\chi}_{ij} + F^{1,\Omega,\chi}_{ij} + F^{1,m,\chi}_{ij}\right]\frac{\varepsilon^{(m)}_\chi}{T} + \mathcal{O}(|\mathbf{B}_\chi|^3) \\ &= G^{0,\chi}_{ij} + G^{1,\Omega,\chi}_{ij} + G^{1,m,\chi}_{ij} + G^{2,\Omega,\chi}_{ij} + G^{2,m,\chi}_{ij} + G^{2,(\Omega,m),\chi}_{ij} + \mathcal{O}(|\mathbf{B}_\chi|^3)\,. \end{aligned} \tag{39}$$

Here,

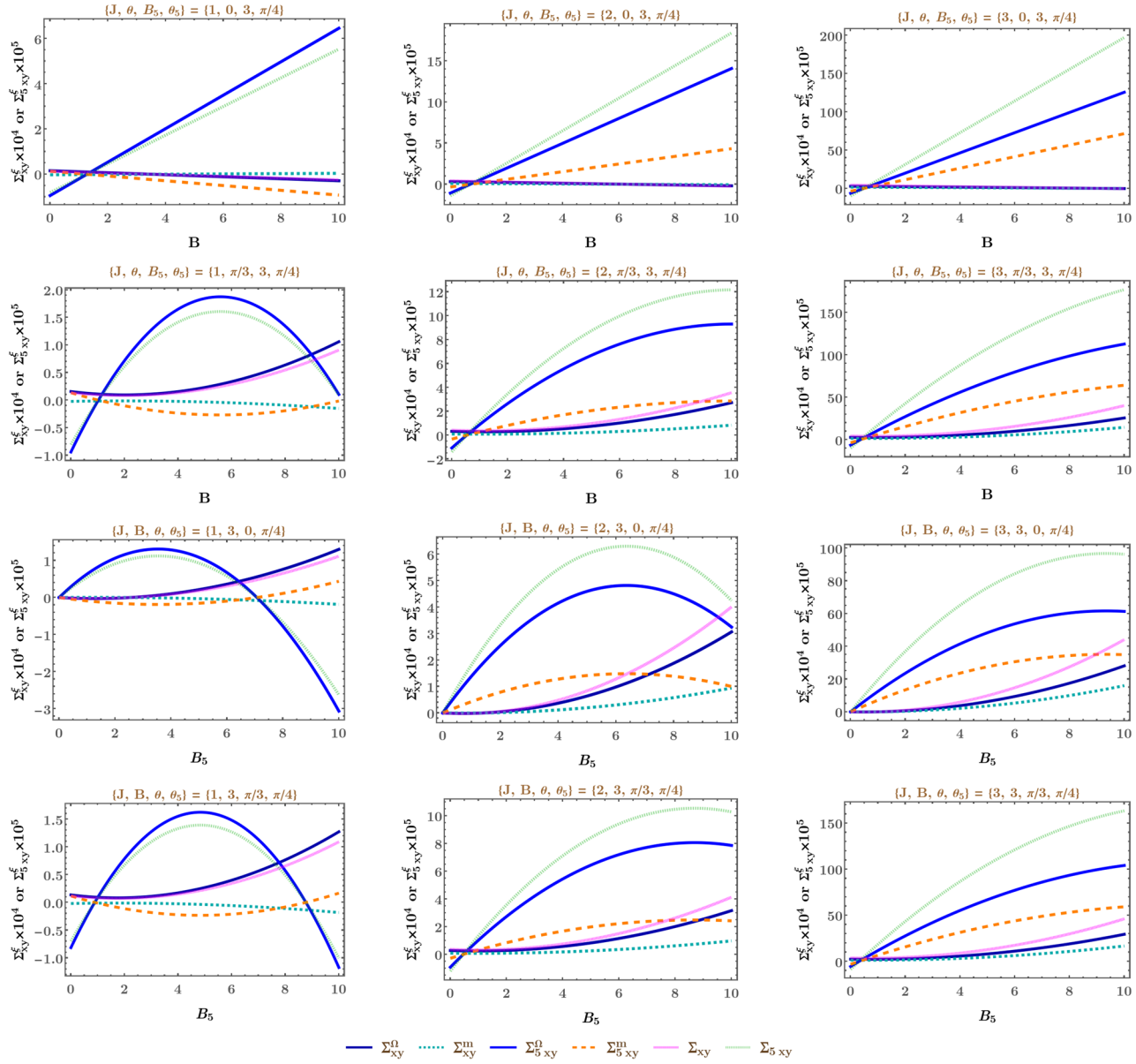

Figure 9. The total and axial combinations of the PHC (in units of eV) for the two conjugate nodes, defined in Eq. (29), as functions of B (in units of eV^2) and B_5 (in units of eV^2), using various values of θ and θ_5 (as indicated in the plotlabels). We have set $v_z = 0.005$, $\tau = 151\,\text{eV}^{-1}$, $\beta = 1160\,\text{eV}^{-1}$, $\mu_+ = 0.4$ eV, and $\mu_- = 0.2$ eV. As explained below Eq. (29), while Σ^{Ω}_{xy} (Σ^{Ω}_{5xy}) represents the part of Σ_{xy} (Σ_{5xy}) originating purely from the BC-contributions (i.e., with no OMM), Σ^{m}_{xy} (Σ^{m}_{5xy}) is the contribution which vanishes if the OMM is neglected. We have used the superscript ξ to indicate that, along the vertical axis, we have plotted the BC-only, OMM, and (BC + OMM) parts, with the colour-coding shown in the plotlegends.

$$
\begin{aligned}
G^{0,\chi}_{ij} &= \frac{F^{0,\chi}_{ij}\,(\varepsilon_\chi - \mu)}{T}\,, \quad G^{1,\Omega,\chi}_{ij} = \frac{F^{1,\Omega,\chi}_{ij}\,(\varepsilon_\chi - \mu)}{T}\,,\\
G^{1,m,\chi}_{ij} &= \frac{F^{0,\chi}_{ij}\,\varepsilon^{(m)}_\chi}{T} + \frac{F^{1,m,\chi}_{ij}\,(\varepsilon_\chi - \mu)}{T}\,, \quad G^{2,\Omega,\chi}_{ij} = \frac{F^{2,\Omega,\chi}_{ij}\,(\varepsilon_\chi - \mu)}{T}\,,\\
G^{2,m,\chi}_{ij} &= \frac{F^{1,m,\chi}_{ij}\,\varepsilon^{(m)}_\chi}{T} + \frac{F^{2,m,\chi}_{ij}\,(\varepsilon_\chi - \mu)}{T}\,, \quad G^{2,(\Omega,m),\chi}_{ij} = \frac{F^{1,\Omega,\chi}_{ij}\,\varepsilon^{(m)}_\chi}{T} + \frac{F^{2,(\Omega,m),\chi}_{ij}\,(\varepsilon_\chi - \mu)}{T}\,,
\end{aligned}
\tag{40}
$$

with the parts named in a similar spirit as done for the case of F^{χ}_{ij}.

Defining a third function $H^{\chi}_{ij} = G_{ij} f_0'(\mathcal{E}_\chi)$, and using Eq. (13), its expansion turns out to be

$$\begin{aligned} H_{ij}^{\chi} &= G_{ij}^{\chi} f_0'(\varepsilon_\chi) + \left[G_{ij}^{0,\chi} + G_{ij}^{1,\Omega,\chi} + G_{ij}^{1,m,\chi}\right] \varepsilon_\chi^{(m)} f_0''(\varepsilon_\chi) + \frac{G_{ij}^{0,\chi}\left(\varepsilon_\chi^{(m)}\right)^2 f_0'''(\varepsilon_\chi)}{2} + \mathcal{O}(|\mathbf{B}_\chi|^3) \\ &= G_{ij}^{0,\chi} + G_{ij}^{1,\Omega,\chi} + G_{ij}^{1,m,\chi} + G_{ij}^{2,\Omega,\chi} + G_{ij}^{2,m,\chi} + G_{ij}^{2,(\Omega,m),\chi} + \mathcal{O}(|\mathbf{B}_\chi|^3)\,. \end{aligned} \tag{41}$$

Here,

$$\begin{aligned} H_{ij}^{0,\chi} &= G_{ij}^{0,\chi} f_0'(\varepsilon_\chi)\,, \quad H_{ij}^{1,\Omega,\chi} = G_{ij}^{1,\Omega,\chi} f_0'(\varepsilon_\chi)\,, \quad H_{ij}^{1,m,\chi} = G_{ij}^{0,\chi}\,\varepsilon_\chi^{(m)} f_0''(\varepsilon_\chi) + G_{ij}^{1,m,\chi} f_0'(\varepsilon_\chi)\,, \\ H_{ij}^{2,\Omega,\chi} &= G_{ij}^{2,\Omega,\chi} f_0'(\varepsilon_\chi)\,, \quad H_{ij}^{2,m,\chi} = \frac{G_{ij}^{0,\chi}\left(\varepsilon_\chi^{(m)}\right)^2 f_0'''(\varepsilon_\chi)}{2} + G_{ij}^{1,m,\chi}\,\varepsilon_\chi^{(m)} f_0''(\varepsilon_\chi) + G_{ij}^{2,m,\chi} f_0'(\varepsilon_\chi)\,, \\ H_{ij}^{2,(\Omega,m),\chi} &= G_{ij}^{1,\Omega,\chi}\,\varepsilon_\chi^{(m)} f_0''(\varepsilon_\chi) + G_{ij}^{2,(\Omega,m),\chi} f_0'(\varepsilon_\chi)\,. \end{aligned} \tag{42}$$

The nomenclature of these parts follow the same scheme as that for F_{ij}^{χ} and G_{ij}^{χ}.

Starting from Eq. (18), applying the weak-in-magnetic-field limit using the expansions outlined above, the expression for the magnetoelectric conductivity tensor α^{χ} is dissociated into

$$\alpha_{ij}^{\chi} = \alpha_{ij}^{0,\chi} + +\alpha_{ij}^{\Omega,\chi} + \alpha_{ij}^{m,\chi}\,, \text{ where } \alpha_{ij}^{\Omega,\chi} = \alpha_{ij}^{1,\Omega,\chi} + \alpha_{ij}^{2,\Omega,\chi}\,, \quad \alpha^{m,\chi} = \alpha_{ij}^{1,m,\chi} + \alpha_{ij}^{2,m,\chi} + \alpha_{ij}^{2,(\Omega,m),\chi}\,. \tag{43}$$

The terms $\alpha_{ij}^{0,\chi}, \alpha_{ij}^{1,\Omega,\chi}, \alpha_{ij}^{2,\Omega,\chi}, \alpha_{ij}^{1,m,\chi}, \alpha_{ij}^{2,m,\chi}$, and $\alpha_{ij}^{2,(\Omega,m),\chi}$ consist of the integrands $H_{ij}^{0,\chi}, H_{ij}^{1,\Omega,\chi}, H_{ij}^{2,\Omega,\chi}, H_{ij}^{1,m,\chi}$, $H_{ij}^{2,m,\chi}$, and $H_{ij}^{2,(\Omega,m),\chi}$, respectively. Analogous to the case of σ_{ij}^{χ}, the term $\alpha_{ij}^{m,\chi}$ goes to zero if the OMM is set to zero.

The longitudinal and transverse components of the magnetothermoelectric conductivity tensor α^{χ} (i.e., the LTEC and the TTEC) are computed from the expressions shown above. The details of the intermediate steps have been relegated to Appendices D and E.

Akin to the magnetoconductivity tensors, we define the total and axial magnetothermoelectric tensors as

$$\alpha_{ij} = \sum_{\chi} \alpha_{ij}^{\chi} \text{ and } \alpha_{5ij} = \sum_{\chi} \chi\, \alpha_{ij}^{\chi}\,, \tag{44}$$

respectively. Subtracting off the $\mathbf{B}_\chi$-independent parts, we define

$$\begin{aligned} A_{ij}(\mathbf{B}_\chi) &= \alpha_{ij}(\mu_+, \mu_-) - \alpha_{ij}(\mu_+, \mu_-)\Big|_{\mathbf{B}_\chi = \mathbf{0}} \\ \text{and } A_{5ij}(\mathbf{B}_\chi) &= \alpha_{5ij}(\mu_+, \mu_-) - \alpha_{5ij}(\mu_+, \mu_-)\Big|_{\mathbf{B}_\chi = \mathbf{0}}. \end{aligned} \tag{45}$$

We denote the parts connected with $\alpha_{ij}^{\Omega,\chi}$ and $\alpha_{ij}^{m,\chi}$ as $(A_{ij}^{\Omega},\ A_{5ij}^{\Omega})$ and $(A_{ij}^{m},\ A_{5ij}^{m})$, respectively. Therefore, if the OMM is not considered, each of $(A_{ij}^{m},\ A_{5ij}^{m})$ goes to zero.

Longitudinal magnetothermoelectric coefficient

Using the explicit expressions derived in Appendix D, we have

$$\alpha_{xx}^{\chi}(\mu_\chi) = \alpha_{xx}^{0,\chi}(\mu_\chi) + \alpha_{xx}^{\Omega,\chi}(\mu_\chi) + \alpha_{xx}^{m,\chi}(\mu_\chi)\,, \tag{46}$$

where

$$\begin{aligned} \alpha_{xx}^{0,\chi}(\mu_\chi) &= -\frac{e\,\tau\,J\,\mu_\chi}{9\,\nu_z\,\beta}\,, \quad \alpha_{xx}^{\Omega,\chi}(\mu_\chi) = \frac{\sqrt{\pi}\,e^3\,\tau\,\nu_z\,\alpha_J^{\frac{2}{J}}\,\Gamma\left(2-\frac{1}{J}\right)}{192\,\beta\,\mu_\chi^{1+\frac{2}{J}}\,\Gamma\left(\frac{9}{2}-\frac{1}{J}\right)}\,\frac{g_x^{bc}\,B_{\chi x}^2 + g_y^{bc}\,B_{\chi y}^2}{J}\,, \\ \alpha_{xx}^{m,\chi}(\mu_\chi) &= \frac{\sqrt{\pi}\,e^3\,\tau\,\nu_z\,\alpha_J^{\frac{2}{J}}\,\Gamma\left(2-\frac{1}{J}\right)}{192\,\mu_\chi^{1+\frac{2}{J}}\,\beta\,\Gamma\left(\frac{9}{2}-\frac{1}{J}\right)}\,\frac{g_x^{m}\,B_{\chi x}^2 + g_y^{m}\,B_{\chi y}^2}{J}\,. \end{aligned} \tag{47}$$

Transverse magnetothermoelectric coefficient

Using the explicit expressions derived in Appendix E, we have

$$\alpha_{yx}^{\chi}(\mu_\chi) = \alpha_{xy}^{\chi}(\mu_\chi) = \alpha_{xy}^{0,\chi}(\mu_\chi) + \alpha_{xy}^{\Omega,\chi}(\mu_\chi) + \alpha_{xy}^{m,\chi}(\mu_\chi)\,, \tag{48}$$

where

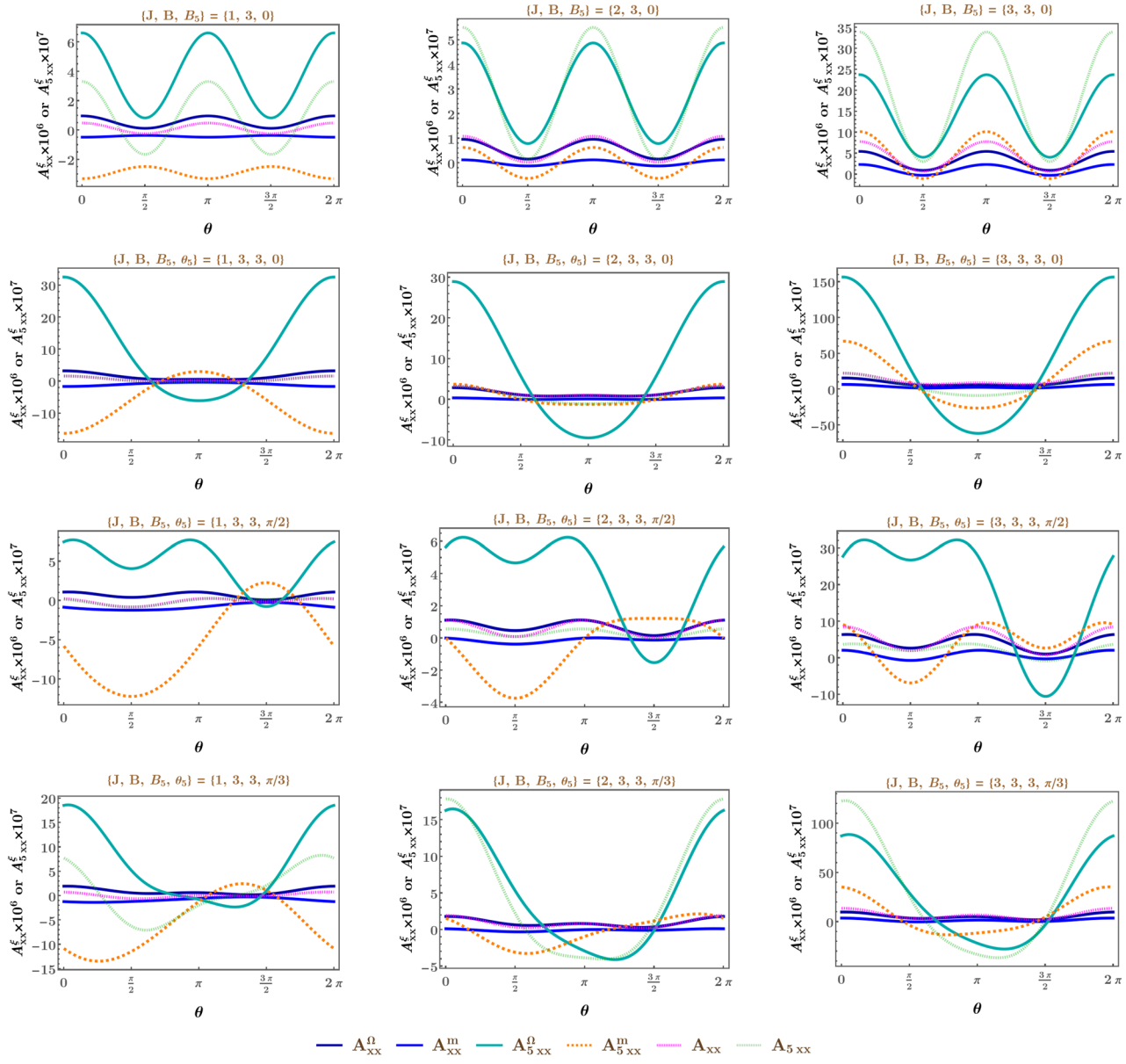

Figure 10. The total and axial combinations of the LTEC (in units of eV) for the two conjugate nodes, defined in Eq. (45), as functions of θ, using various values of B (in units of eV^2), B_5 (in units of eV^2), and θ_5 (as indicated in the plotlabels). We have set $v_z = 0.005$, $\tau = 151\,\mathrm{eV}^{-1}$, $\beta = 1160\,\mathrm{eV}^{-1}$, $\mu_+ = 0.2$ eV, and $\mu_- = 0.35$ eV. As explained below Eq. (45), while A^{Ω}_{xx} (A^{Ω}_{5xx}) represents the part of A_{xx} (A_{5xx}) originating purely from the BC-contributions (i.e., with no OMM), A^{m}_{xx} (A^{m}_{5xx}) is the contribution which vanishes if OMM is not at all considered. We have used the superscript ξ to indicate that, along the vertical axis, we have plotted the BC-only, OMM, and (BC + OMM) parts, with the colour-coding shown in the plotlegends. The values of the maxima and minima of the curves are strongly dependent on the values of J.

$$\alpha^{0,\chi}_{xy}(\mu_\chi) = 0\,, \quad \alpha^{\Omega,\chi}_{xy}(\mu_\chi) = \frac{\sqrt{\pi}\, e^3\, \tau\, v_z\, \alpha_J^{\frac{2}{J}}\, \Gamma\left(2-\frac{1}{J}\right)}{96\,\beta\,\mu_\chi^{1+\frac{2}{J}}\,\Gamma\left(\frac{9}{2}-\frac{1}{J}\right)}\,\frac{f^{bc}(J)}{J}\,B_{\chi x}\,B_{\chi y}\,,$$
$$\alpha^{m,\chi}_{xy}(\mu_\chi) = \frac{\sqrt{\pi}\, e^3\, \tau\, v_z\, \alpha_J^{\frac{2}{J}}\, \Gamma\left(2-\frac{1}{J}\right)}{96\,\beta\,\mu_\chi^{1+\frac{2}{J}}\,\Gamma\left(\frac{9}{2}-\frac{1}{J}\right)}\,\frac{f^{m}(J)}{J}\,B_{\chi x}\,B_{\chi y}\,. \tag{49}$$

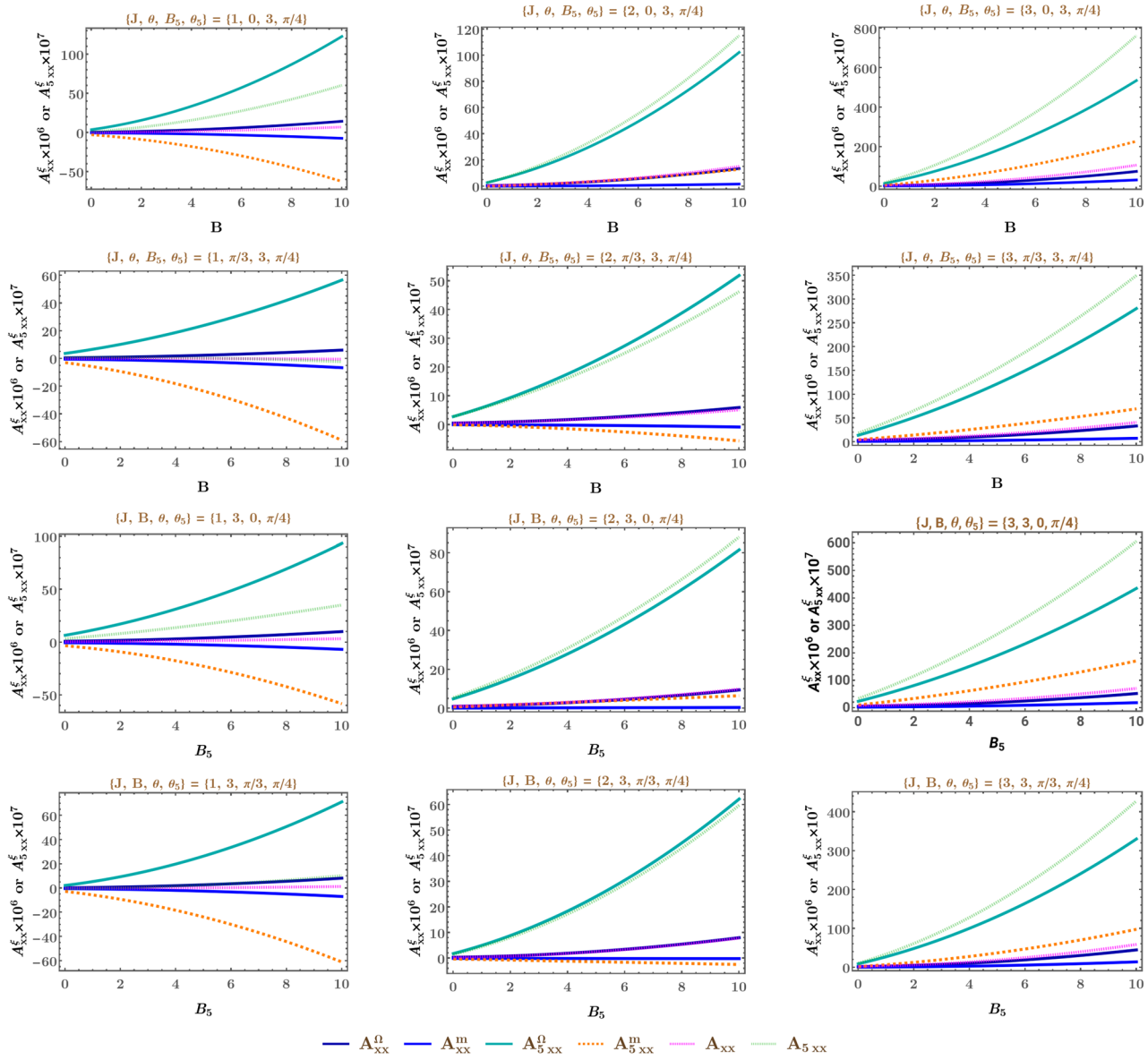

Figure 11. The total and axial combinations of the LTEC (in units of eV) for the two conjugate nodes, defined in Eq. (45), as functions of B (in units of eV^2) and B_5 (in units of eV^2), using various values of θ and θ_5 (as indicated in the plotlabels). We have set $v_z = 0.005$, $\tau = 151\,\mathrm{eV}^{-1}$, $\beta = 1160\,\mathrm{eV}^{-1}$, $\mu_+ = 0.2$ eV, and $\mu_- = 0.35$ eV. As explained below Eq. (45), while A^{Ω}_{xx} (A^{Ω}_{5xx}) represents the part of A_{xx} (A_{5xx}) originating purely from the BC-contributions (i.e., with no OMM), A^{m}_{xx} (A^{m}_{5xx}) is the contribution which vanishes if the OMM is neglected. We have used the superscript ξ to indicate that, along the vertical axis, we have plotted the BC-only, OMM, and (BC + OMM) parts, with the colour-coding shown in the plotlegends.

Mott relation

From the explicit expressions of the in-plane longitudinal and transverse components of σ^{χ} and α^{χ}, which we have derived [cf. Eqs. (31), (34), (47), and (49)], we can immediately infer that the relation

$$\partial_{\mu_\chi}\sigma^{\chi}_{ij}(\mu_\chi) = -\frac{3\,e\,\beta}{\pi^2}\,\alpha^{\chi}_{ij}(\mu_\chi) + \mathcal{O}(\beta^{-2}) \tag{50}$$

is satisfied. This is equivalent to satisfying the Mott relation $\alpha^{\chi}_{ij}(\mu_\chi) = -\frac{\pi^2}{3\,e\,\beta}\,\partial_{\mu_\chi}\sigma^{\chi}_{ij}(\mu_\chi)$, which holds in the limit $\beta \to \infty$[57], and can be derived mathematically through the Sommerfeld expansion. Hence, we find that the Mott relation continues to hold even in the presence of OMM, agreeing with the results in Ref.59, where generic settings have been considered.

Due to the Mott relation, the nature of A^{Ω}_{ij} and A^{m}_{ij} can be readily inferred from that of Σ^{Ω}_{ij} and Σ^{m}_{ij}, which we have already discussed in the preceding section. Nevertheless, we provide here some representative plots of the (1) longitudinal planar components A^{Ω}_{xx}, A^{m}_{xx}, A^{Ω}_{5xx}, and A^{m}_{5xx} in Figs. 10 and 11; (2) transverse planar components

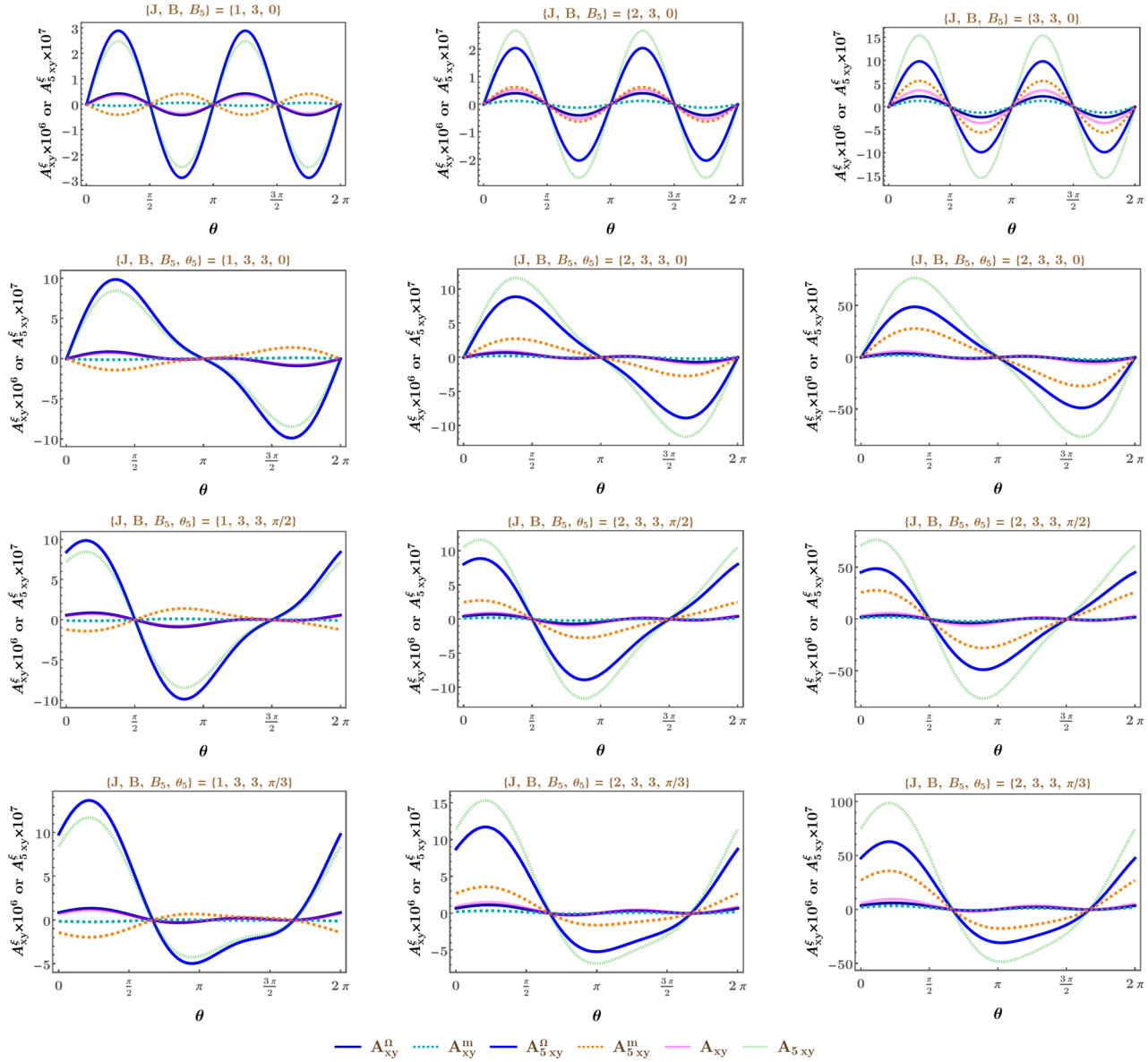

Figure 12. The total and axial combinations of the TTEC (in units of eV) for the two conjugate nodes, defined in Eq. (45), as functions of θ, using various values of B (in units of eV^2), B_5 (in units of eV^2), and θ_5 (as indicated in the plotlabels). We have set $\nu_z = 0.005$, $\tau = 151\,\text{eV}^{-1}$, $\beta = 1160\,\text{eV}^{-1}$, $\mu_+ = 0.2$ eV, and $\mu_- = 0.35$ eV. As explained below Eq. (45), while A^{Ω}_{xy} (A^{Ω}_{5xy}) represents the part of A_{xy} (A_{5xy}) originating purely from the BC-contributions (i.e., with no OMM), A^{m}_{xy} (A^{m}_{5xy}) is the contribution which vanishes if OMM is not at all considered. We have used the superscript ξ to indicate that, along the vertical axis, we have plotted the BC-only, OMM, and (BC + OMM) parts, with the colour-coding shown in the plotlegends. The values of the maxima and minima of the curves are strongly dependent on the values of J.

A^{Ω}_{xy}, A^{m}_{xy}, A^{Ω}_{5xy}, and A^{m}_{5xy} in Figs. 12 and 13. We choose a different set of values for μ_+ and μ_-, compared to those chosen for Figs. 6, 7, 8, 9, so as to cover a somewhat different parameter range for illustrative purposes. In fact, we have chosen here $\mu_+ - \mu_- < 0$, compared to the chosen value of $\mu_+ - \mu_- > 0$ for the earlier section, which leads to a sign-flip of the cyan, orange, and light-green curves representing the axial combinations of the response tensors.

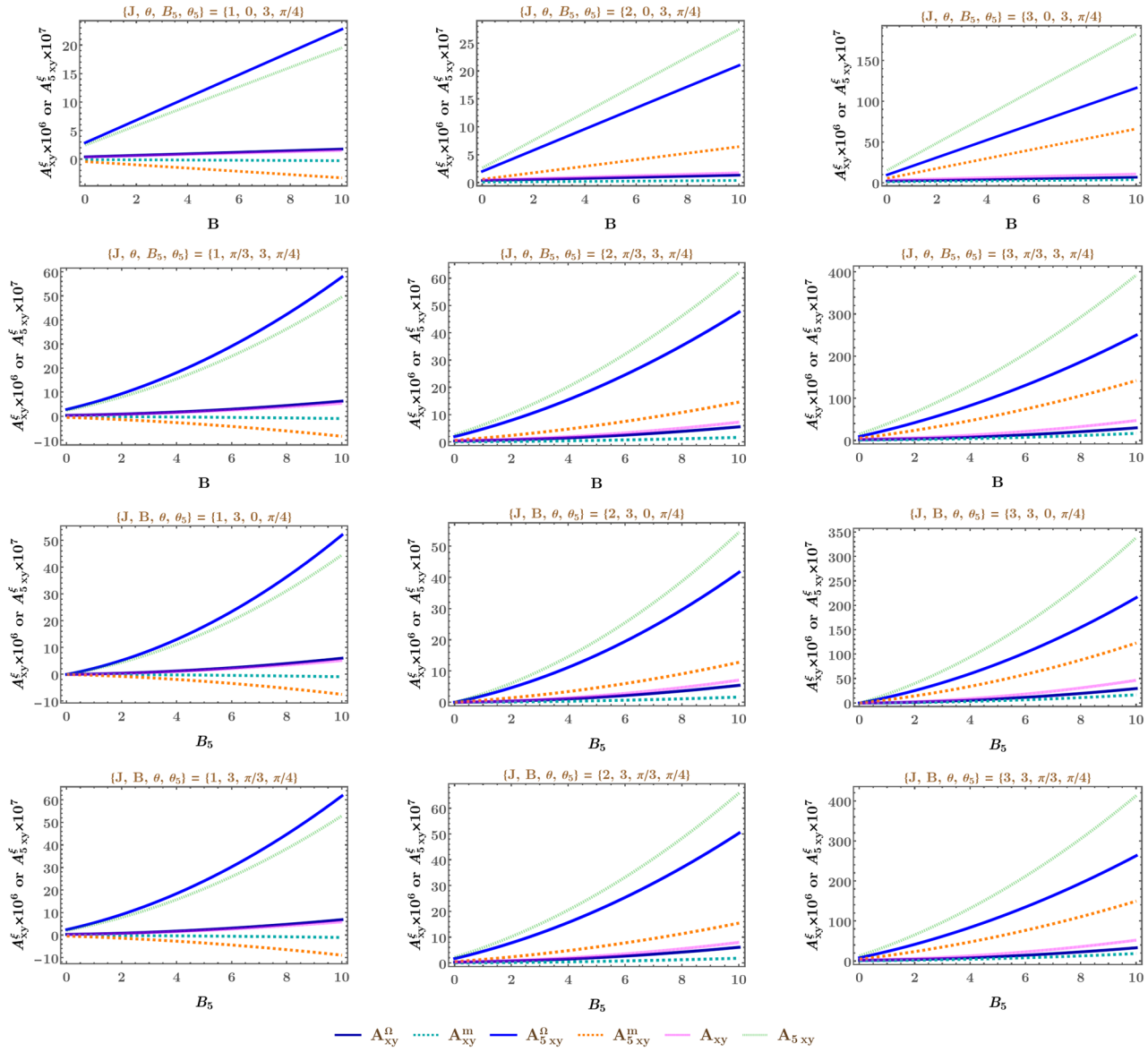

Figure 13. The total and axial combinations of the TTEC (in units of eV) for the two conjugate nodes, defined in Eq. (45), as functions of B (in units of eV^2) and B_5 (in units of eV^2), using various values of θ and θ_5 (as indicated in the plotlabels). We have set $v_z = 0.005$, $\tau = 151\,\mathrm{eV}^{-1}$, $\beta = 1160\,\mathrm{eV}^{-1}$, $\mu_+ = 0.2$ eV, and $\mu_- = 0.35$ eV. As explained below Eq. (45), while A^{Ω}_{xy} (A^{Ω}_{5xy}) represents the part of A_{xy} (A_{5xy}) originating purely from the BC-contributions (i.e., with no OMM), A^{m}_{xy} (A^{m}_{5xy}) is the contribution which vanishes if the OMM is neglected. We have used the superscript ξ to indicate that, along the vertical axis, we have plotted the BC-only, OMM, and (BC + OMM) parts, with the colour-coding shown in the plotlegends.

Magnetothermal coefficient

Using the function F_{ij}, whose Taylor-expanded form has been shown in Eq. (37), we now define the function $\tilde{G}^{\chi}_{ij} = F^{\chi}_{ij}\left(\mathcal{E}_{\chi}-\mu\right)^2/T = F^{\chi}_{ij}\left[\varepsilon_{\chi}+\varepsilon^{(m)}_{\chi}-\mu\right]^2/T$. Its weak-field expansion is given by

$$\begin{aligned}\tilde{G}^{\chi}_{ij} &= F^{\chi}_{ij}\frac{\left(\varepsilon_{\chi}-\mu\right)^2}{T} + 2\left[F^{0,\chi}_{ij}+F^{1,\Omega,\chi}_{ij}+F^{1,m,\chi}_{ij}\right]\frac{\left(\varepsilon_{\chi}-\mu\right)\varepsilon^{(m)}_{\chi}}{T} + F^{0,\chi}_{ij}\frac{\left(\varepsilon^{(m)}_{\chi}\right)^2}{T} + \mathcal{O}(|\mathbf{B}_{\chi}|^3) \\ &= \tilde{G}^{0,\chi}_{ij} + \tilde{G}^{1,\Omega,\chi}_{ij} + G^{1,m,\chi}_{ij} + \tilde{G}^{2,\Omega,\chi}_{ij} + \tilde{G}^{2,m,\chi}_{ij} + \tilde{G}^{2,(\Omega,m),\chi}_{ij} + \mathcal{O}(|\mathbf{B}_{\chi}|^3)\,.\end{aligned} \tag{51}$$

Here,

$$
\begin{aligned}
\tilde{G}_{ij}^{0,\chi} &= \frac{F_{ij}^{0,\chi}\left(\varepsilon_\chi-\mu\right)^2}{T}\,,\\
\tilde{G}_{ij}^{1,\Omega,\chi} &= \frac{F_{ij}^{1,\Omega,\chi}\left(\varepsilon_\chi-\mu\right)^2}{T}\,,\\
\tilde{G}_{ij}^{1,m,\chi} &= \frac{2\,F_{ij}^{0,\chi}\left(\varepsilon_\chi-\mu\right)\varepsilon_\chi^{(m)}}{T}+\frac{F_{ij}^{1,m,\chi}\left(\varepsilon_\chi-\mu\right)^2}{T}\,,\\
\tilde{G}_{ij}^{2,\Omega,\chi} &= \frac{F_{ij}^{2,\Omega,\chi}\left(\varepsilon_\chi-\mu\right)^2}{T}\,,\\
\tilde{G}_{ij}^{2,m,\chi} &= \frac{2\,F_{ij}^{1,m,\chi}\left(\varepsilon_\chi-\mu\right)\varepsilon_\chi^{(m)}}{T}+\frac{F_{ij}^{2,m,\chi}\left(\varepsilon_\chi-\mu\right)^2}{T}+\frac{F_{ij}^{0,\chi}\left(\varepsilon_\chi^{(m)}\right)^2}{T}\,,\\
\tilde{G}_{ij}^{2,(\Omega,m),\chi} &= \frac{2\,F_{ij}^{1,\Omega,\chi}\left(\varepsilon_\chi-\mu\right)\varepsilon_\chi^{(m)}}{T}+\frac{F_{ij}^{2,(\Omega,m),\chi}\left(\varepsilon_\chi-\mu\right)^2}{T}\,.
\end{aligned}
\tag{52}
$$

We need to define one last function $\tilde{H}_{ij}^{\chi}=\tilde{G}_{ij}f_0'(\mathcal{E}_\chi)$. Using Eq. (13), its expansion turns out to be

$$
\begin{aligned}
\tilde{H}_{ij}^{\chi} &= \tilde{G}_{ij}^{\chi}f_0'(\varepsilon_\chi)+\left[\tilde{G}_{ij}^{0,\chi}+\tilde{G}_{ij}^{1,\Omega,\chi}+\tilde{G}_{ij}^{1,m,\chi}\right]\varepsilon_\chi^{(m)}f_0''(\varepsilon_\chi)+\frac{\tilde{G}_{ij}^{0,\chi}\left(\varepsilon_\chi^{(m)}\right)^2f_0'''(\varepsilon_\chi)}{2}+\mathcal{O}(|\mathbf{B}_\chi|^3)\\
&= \tilde{G}_{ij}^{0,\chi}+\tilde{G}_{ij}^{1,\Omega,\chi}+\tilde{G}_{ij}^{1,m,\chi}+\tilde{G}_{ij}^{2,\Omega,\chi}+\tilde{G}_{ij}^{2,m,\chi}+\tilde{G}_{ij}^{2,(\Omega,m),\chi}+\mathcal{O}(|\mathbf{B}_\chi|^3)\,,
\end{aligned}
\tag{53}
$$

where

$$
\begin{aligned}
&\tilde{H}_{ij}^{0,\chi}=\tilde{G}_{ij}^{0,\chi}f_0'(\varepsilon_\chi)\,,\quad \tilde{H}_{ij}^{1,\Omega,\chi}=\tilde{G}_{ij}^{1,\Omega,\chi}f_0'(\varepsilon_\chi)\,,\\
&\tilde{H}_{ij}^{1,m,\chi}=\tilde{G}_{ij}^{0,\chi}\,\varepsilon_\chi^{(m)}f_0''(\varepsilon_\chi)+\tilde{G}_{ij}^{1,m,\chi}f_0'(\varepsilon_\chi)\,,\quad \tilde{H}_{ij}^{2,\Omega,\chi}=\tilde{G}_{ij}^{2,\Omega,\chi}f_0'(\varepsilon_\chi)\,,\\
&\tilde{H}_{ij}^{2,m,\chi}=\frac{\tilde{G}_{ij}^{0,\chi}\left(\varepsilon_\chi^{(m)}\right)^2f_0'''(\varepsilon_\chi)}{2}+\tilde{G}_{ij}^{1,m,\chi}\,\varepsilon_\chi^{(m)}f_0''(\varepsilon_\chi)+\tilde{G}_{ij}^{2,m,\chi}f_0'(\varepsilon_\chi)\,,\\
&\tilde{H}_{ij}^{2,(\Omega,m),\chi}=\tilde{G}_{ij}^{1,\Omega,\chi}\,\varepsilon_\chi^{(m)}f_0''(\varepsilon_\chi)+\tilde{G}_{ij}^{2,(\Omega,m),\chi}f_0'(\varepsilon_\chi)\,.
\end{aligned}
\tag{54}
$$

Using the expressions shown above, the integrand in Eq. (19) is expanded in the weak-in-magnetic-field limit, leading to

$$
\ell_{ij}^{\chi}=\ell_{ij}^{0,\chi}++\ell_{ij}^{\Omega,\chi}+\ell_{ij}^{m,\chi},\ \text{where}\ \ell_{ij}^{\Omega,\chi}=\ell_{ij}^{1,\Omega,\chi}+\ell_{ij}^{2,\Omega,\chi}\,,\quad \ell_{ij}^{m,\chi}=\ell_{ij}^{1,m,\chi}+\ell_{ij}^{2,m,\chi}+\ell_{ij}^{2,(\Omega,m),\chi}\,. \tag{55}
$$

Analogous to α_{ij}^{χ}, the terms $\ell_{ij}^{0,\chi}$, $\ell_{ij}^{1,\Omega,\chi}$, $\ell_{ij}^{2,\Omega,\chi}$, $\ell_{ij}^{1,m,\chi}$, $\ell_{ij}^{2,m,\chi}$, and $\ell_{ij}^{2,(\Omega,m),\chi}$ have been labelled such that they are defined by the integrands $\tilde{H}_{ij}^{0,\chi}$, $\tilde{H}_{ij}^{1,\Omega,\chi}$, $\tilde{H}_{ij}^{2,\Omega,\chi}$, $\tilde{H}_{ij}^{1,m,\chi}$, $\tilde{H}_{ij}^{2,m,\chi}$, and $\tilde{H}_{ij}^{2,(\Omega,m),\chi}$, respectively. Analogous to the cases of σ_{ij}^{χ} and α_{ij}^{χ}, the term $\ell_{ij}^{m,\chi}$ goes to zero if the OMM is set to zero.

The expressions are cumbersome and, hence, it is useful to break them up into smaller bits. In particular, we define

$$
\ell_{ij}^{2,m,\chi}=I_{1,ij}^{\ell,2}+I_{2,ij}^{\ell,2}+I_{3,ij}^{\ell,2}\,, \tag{56}
$$

where

$$
\begin{aligned}
I_{1,ij}^{\ell,2} &= -\tau\int\frac{d^3\mathbf{k}}{(2\pi)^3}\left[v_{\chi i}^{(0)}v_{\chi j}^{(0)}\frac{\left(\varepsilon_\chi^{(m)}\right)^2}{T}+2\left(v_{\chi i}^{(0)}v_{\chi j}^{(m)}+v_{\chi i}^{(m)}v_{\chi j}^{(0)}\right)\frac{\left(\varepsilon_\chi-\mu\right)\varepsilon_\chi^{(m)}}{T}\right.\\
&\qquad\left.+\,v_{\chi i}^{(m)}v_{\chi j}^{(m)}\frac{\left(\varepsilon_\chi-\mu\right)^2}{T}\right]f_0'(\varepsilon_\chi)\,,\\
I_{2,ij}^{\ell,2} &= -\tau\int\frac{d^3\mathbf{k}}{(2\pi)^3}\left[\left(v_{\chi i}^{(0)}v_{\chi j}^{(m)}+v_{\chi i}^{(m)}v_{\chi j}^{(0)}\right)\frac{\left(\varepsilon_\chi-\mu\right)^2\varepsilon_\chi^{(m)}}{T}\right.\\
&\qquad\left.+\,2\,v_{\chi i}^{(0)}v_{\chi j}^{(0)}\frac{\left(\varepsilon_\chi-\mu\right)\left(\varepsilon_\chi^{(m)}\right)^2}{T}\right]f_0''(\varepsilon_\chi)\,,\\
I_{3,ij}^{\ell,2} &= -\tau\int\frac{d^3\mathbf{k}}{(2\pi)^3}\frac{v_{\chi i}^{(0)}v_{\chi j}^{(0)}}{2}\frac{\left(\varepsilon_\chi-\mu\right)^2\left(\varepsilon_\chi^{(m)}\right)^2}{T}f_0'''(\varepsilon_\chi)\,.
\end{aligned}
\tag{57}
$$

In a similar spirit, we define

$$\ell_{ij}^{2,(m,\Omega),\chi} = I_{1,ij}^{\ell,3} + I_{2,ij}^{\ell,3} + I_{3,ij}^{\ell,3}, \tag{58}$$

with

$$\begin{aligned}
I_{1,ij}^{\ell,3} &= -2\,e\,\tau \int \frac{d^3\mathbf{k}}{(2\,\pi)^3}\, f_0'(\varepsilon_\chi)\, \frac{(\varepsilon_\chi - \mu)\,\varepsilon_\chi^{(m)}}{T} \\
&\qquad \times \Big[\Big(\boldsymbol{v}_\chi^{(0)} \cdot \boldsymbol{\Omega}_\chi\Big)\Big(v_{\chi i}^{(0)}\, B_{\chi j} + B_{\chi i}\, v_{\chi j}^{(0)}\Big) - \big(\mathbf{B}_\chi \cdot \boldsymbol{\Omega}_\chi\big)\, v_{\chi i}^{(0)}\, v_{\chi j}^{(0)}\Big], \\
I_{2,ij}^{\ell,3} &= -e\,\tau \int \frac{d^3\mathbf{k}}{(2\,\pi)^3} \Big[\Big(\boldsymbol{v}_\chi^{(0)} \cdot \boldsymbol{\Omega}_\chi\Big)\Big(v_{\chi i}^{(m)}\, B_{\chi j} + B_{\chi i}\, v_{\chi j}^{(m)}\Big) + \Big(\boldsymbol{v}_\chi^{(m)} \cdot \boldsymbol{\Omega}_\chi\Big)\Big(v_{\chi i}^{(0)}\, B_{\chi j} + B_{\chi i}\, v_{\chi j}^{(0)}\Big) \\
&\qquad - \big(\mathbf{B}_\chi \cdot \boldsymbol{\Omega}_\chi\big)\Big(v_{\chi i}^{(0)}\, v_{\chi j}^{(m)} + v_{\chi i}^{(m)}\, v_{\chi j}^{(0)}\Big)\Big]\, \frac{(\varepsilon_\chi - \mu)^2}{T} f_0'(\varepsilon_\chi), \\
I_{3,ij}^{\ell,3} &= -e\,\tau \int \frac{d^3\mathbf{k}}{(2\,\pi)^3} \Big[\Big(\boldsymbol{v}_\chi^{(0)} \cdot \boldsymbol{\Omega}_\chi\Big)\Big(v_{\chi i}^{(0)}\, B_{\chi j} + B_{\chi i}\, v_{\chi j}^{(0)}\Big) - \big(\mathbf{B}_\chi \cdot \boldsymbol{\Omega}_\chi\big)\, v_{\chi i}^{(0)}\, v_{\chi j}^{(0)}\Big]\, \frac{(\varepsilon_\chi - \mu)^2 \varepsilon_\chi^{(m)}}{T} f_0''(\varepsilon_\chi).
\end{aligned} \tag{59}$$

The longitudinal and transverse components of the tensor ℓ^χ are computed from the expressions shown above, in the same way as we have done for σ^χ and α^χ. The details of the intermediate steps have been relegated to Appendices F and G.

Longitudinal magnetothermal coefficient

Using the explicit expressions derived in Appendix F, we have

$$\ell_{xx}^{\chi}(\mu_\chi) = \ell_{xx}^{0,\chi}(\mu_\chi) + \ell_{xx}^{\Omega,\chi}(\mu_\chi) + \ell_{xx}^{m,\chi}(\mu_\chi), \tag{60}$$

where

$$\begin{aligned}
\ell_{xx}^{0,\chi}(\mu_\chi) &= \frac{J\,\tau\,\mu_\chi^2\,T}{18\,v_z}, \\
\ell_{xx}^{\Omega,\chi}(\mu_\chi) &= \frac{\sqrt{\pi}\,e^2\,\tau\,v_z\,\alpha_J^{\frac{2}{J}}\,T}{3\times 128\,\mu_\chi^{\frac{2}{J}}}\, \frac{\Gamma\big(2-\frac{1}{J}\big)}{\Gamma\big(\frac{9}{2}-\frac{1}{J}\big)}\Big[g_x^{bc}(J)\,B_{\chi x}^2 + g_y^{bc}(J)\,B_{\chi y}^2\Big], \\
\ell_{xx}^{m,\chi}(\mu_\chi) &= \frac{\sqrt{\pi}\,e^2\,\tau\,v_z\,\alpha_J^{\frac{2}{J}}\,T}{3\times 128\,\mu_\chi^{\frac{2}{J}}}\, \frac{\Gamma\big(2-\frac{1}{J}\big)}{\Gamma\big(\frac{9}{2}-\frac{1}{J}\big)}\Big[g_x^{m}(J)\,B_{\chi x}^2 + g_y^{m}(J)\,B_{\chi y}^2\Big].
\end{aligned} \tag{61}$$

Transverse magnetothermal coefficient

Using the explicit expressions derived in Appendix G, we have

$$\ell_{yx}^{\chi}(\mu_\chi) = \ell_{xy}^{\chi}(\mu_\chi) = \ell_{xy}^{0,\chi}(\mu_\chi) + \ell_{xy}^{\Omega,\chi}(\mu_\chi) + \ell_{xy}^{m,\chi}(\mu_\chi), \tag{62}$$

where

$$\begin{aligned}
\ell_{xy}^{0,\chi}(\mu_\chi) &= 0, \\
\ell_{xy}^{\Omega,\chi}(\mu_\chi) &= \frac{\sqrt{\pi}\,e^2\,\tau\,v_z\,\alpha_J^{\frac{2}{J}}\,T}{3\times 64\,\mu_\chi^{\frac{2}{J}}}\, \frac{\Gamma\big(2-\frac{1}{J}\big)}{\Gamma\big(\frac{9}{2}-\frac{1}{J}\big)}\, f^{bc}(J)\,B_{\chi x}\,B_{\chi y}, \\
\ell_{xy}^{m,\chi}(\mu_\chi) &= \frac{\sqrt{\pi}\,e^2\,\tau\,v_z\,\alpha_J^{\frac{2}{J}}\,T}{3\times 64\,\mu_\chi^{\frac{2}{J}}}\, \frac{\Gamma\big(2-\frac{1}{J}\big)}{\Gamma\big(\frac{9}{2}-\frac{1}{J}\big)}\, f^{m}(J)\,B_{\chi x}\,B_{\chi y}.
\end{aligned} \tag{63}$$

Wiedemann-Franz law

From the explicit expressions of the in-plane longitudinal and transverse components of σ^χ and ℓ^χ, which we have derived [cf. Eqs. (31), (34), (61), and (62)], we immediately find that the relation

$$\sigma_{ij}^{\chi} = \frac{3\,e^2}{\pi^2\,T}\,\ell_{ij}^{\chi} + \mathcal{O}(\beta^{-2}) \tag{64}$$

is satisfied. This is equivalent to satisfying the Wiedemann-Franz law, which holds in the limit $\beta \to \infty$[57]. Hence, we have demonstrated that the Wiedemann-Franz law continues to hold even in the presence of OMM. This relation tells us that, knowing the nature of the magnetoelectric conductivity, we can infer the behaviour of the magnetothermal coefficient. Therefore, it is not necessary to provide any separate plots for this response.

Summary and future perspectives

In this paper, we have considered planar Hall (or planar thermal Hall) configurations such that a 3d Weyl or multi-Weyl semimetal is subjected to a conjunction of an electric field $\mathbf{E}$ (and/or temperature gradient $\nabla_{\mathbf{r}} T$) and an effective magnetic field $\mathbf{B}_\chi$, oriented at a generic angle with respect to each other. The z-axis is chosen to be along the direction along which the mWSM shows a linear-in-momentum dispersion, and is perpendicular to the plane of $\mathbf{E}$ (or $\nabla_{\mathbf{r}} T$) and $\mathbf{B}_\chi$. The effective magnetic field consists of two parts — (a) an actual/physical magnetic field $\mathbf{B}$, and (b) an emergent magnetic field $\mathbf{B}_5$ which arises if the sample is subjected to elastic deformations (strain tensor field). Since $\mathbf{B}_5$ exhibits a chiral nature, because it couples to conjugate nodal points of opposite chiralities with opposite signs, $\mathbf{B}_\chi$ is given by $\mathbf{B} + \chi\, \mathbf{B}_5$. The relative orientations of these two constituents of $\mathbf{B}_\chi$, with respect to the direction of the electric field (or temperature gradient), give rise to a rich variety of possibilities in the characteristics of the electric, thermal, and thermoelectric response tensors. We have derived explicit expressions for these response coefficients, which have helped us to identify unambiguously the interplay of the BC- and OMM-contributions. In addition, we have illustrated the overall behaviour of the response in some realistic parameter regimes. We have found that the total (i.e., sum) and the axial (i.e., difference) combinations of the response, from the two conjugate nodes, depend strongly on the specific value of J. In particular, for the planar transverse components of the response tensors, while the OMM part acts exclusively in opposition with the BC-only part for the Weyl semimetals, the former syncs with the latter for $J > 1$, thereby enhancing the overall response. The strain-induced $\mathbf{B}_5$ provides a way to have linear-in-B terms in the response coefficients for untilted nodes, in addition to the quadratic-in-B dependence.

The B^2-dependence and the π-periodic behaviour (with respect to θ) of the magnetoelectric conductivity in the absence of B_5 have been observed in numerous experiments, which involve materials like $ZrTe_5$[60], TaAs[61], NbP and NbAs[17], and $Co_3Sn_2S_2$[62], known to host Weyl nodes. Furthermore, the magnetothermal coefficient has also been measured in materials such as NdAlSi[63], which again shows the expected B^2-dependence. It is possible to modify these experimental set-ups to devise the mechanism for applying strain gradients to the samples, thus leading to the realization of B_5[64] in addition.

For the case of a negative chemical potential, we need to focus on the valence band at the corresponding node. The energy, band velocity, and Berry curvature will have opposite signs compared to the case of the positive chemical potential. For the magnetic-field-independent "Drude" parts, we have found that, independent of the J-values, $\sigma_{xx}^{0,\chi}(\mu_\chi)$ and $\ell_{xx}^{0,\chi}(\mu_\chi)$ are proportional to μ_χ^2, while $\alpha_{xx}^{0,\chi}(\mu_\chi) \propto \mu_\chi$. For the magnetic-field-dependent parts, the leading-order μ_χ-dependence goes as (i) $\mu_\chi^{-\frac{2}{J}}$ for σ_{ij}^{χ}, (ii) $\mu_\chi^{-1-\frac{2}{J}}$ for α_{ij}^{χ}, and (iii) $\mu^{\frac{2}{J}}$ for ℓ_{ij}^{χ}. Hence, for $J = 3$, the non-Drude parts depend on a fractional power of μ_χ, which physically makes no sense for $\mu_\chi < 0$. Now we must remember that, in our formalism, we have not included μ_χ in the starting Hamiltonian $\mathcal{H}_\chi$, but have included it in the Fermi distribution function. This has allowed us to derive analytical expressions by applying the Sommerfeld expansion, and the form of the final expressions (summarized above) are an artifact of our specific procedure. Therefore, we conclude that it is possible to derive the results for $\mu_\chi < 0$ by implementing the same procedure, but considering the transport contributed by a valence band (with the sign changes quoted above), for $J = 1, 2$. However, it will not work for $J = 3$ due to the presence of fractional powers of μ_χ. The results for $J = 1, 2$ are thus expected to have a dependence on the various parameters similar to the $\mu_\chi > 0$ case that we have considered here, modulo possible minus signs for the various contributing parts. As for the $J = 3$ case, we can include the negative chemical potential at the Hamiltonian level, such that it directly enters into the energy eigenvalue expressions, and then numerically evaluate the behaviour of the various response tensors.

In Refs.[27,28], the authors have included a momentum-independent internode scattering time τ_v, in addition to the intranode scattering time τ. The inclusion of the internode processes results in stabilizing the chiral anomaly, as it inherently leads to different chemical potentials in the two conjugate WSM/mWSM nodes. By plugging in τ_v as a phenomenological constant (because of ignoring its momentum dependence), Ref.27 has considered the resulting semiclassical Boltzmann equations for the two nodes in an untilted WSM. The authors have shown that a finite τ_v is tied to a difference in the chemical potential between the two nodes, given by $\Delta\mu \propto (\mathbf{E} \cdot \mathbf{B})\tau_v$ (in the absence of a pseudomagnetic field). They have inferred that this results in the magnetoelectric conductivity tensor components acquiring extra contributions $\propto \tau_v$ and normal physical conditions dictate that $\tau_v \gg \tau$. The same behaviour is found for the case of the thermoelectric conductivity tensor. A more complete treatment can be found in[36], where the authors do not assume a momentum-independent internode-scattering time, and they go beyond the relaxation-time approximation. It remains to be seen how the above calculations pan out for the mWSMs and multifold semimetals[65], and what are the forms of the resulting final expressions.

In the future, it will be worthwhile to perform the same calculations by including tilted nodes[27,28,36,39], because tilting is applicable for generic scenarios. A tilt can induce terms which are linearly-dependent on B, even in the absence of a strain-induced $\mathbf{B}_5$-part. Furthermore, a more realistic calculational set-up should include internode scatterings[28] and going beyond the relaxation-time approximation[36]. Although we have considered the weak-magnetic-field scenario in this paper, under the influence of a strong quantizing magnetic field, we have to incorporate the effects of the discrete Landau levels while computing the linear response[33,66–68]. Other auxiliary directions include the study of linear and nonlinear response in the presence of disorder and/or strong correlations[69–76]. One could also explore the effects of a time-periodic drive[21,77,78], for instance, by shining circularly polarized light.

Data availibility

All data generated or analysed during this study are included in this published article.

Received: 4 June 2024; Accepted: 25 July 2024
Published online: 13 September 2024

References

1. Burkov, A. A. & Balents, L. Weyl semimetal in a topological insulator multilayer. *Phys. Rev. Lett.* **107**, 127205. https://doi.org/10.1103/PhysRevLett.107.127205 (2011).
2. Yan, B. & Felser, C. Topological materials: Weyl semimetals. *Annu. Rev. Condens. Matter Phys.* **8**, 337. https://doi.org/10.1146/annurev-conmatphys-031016-025458 (2017).
3. Bradlyn, B. *et al.* Beyond Dirac and Weyl fermions: Unconventional quasiparticles in conventional crystals. *Science* **353**, aaf5037 (2016).
4. Fang, C., Gilbert, M. J., Dai, X. & Bernevig, B. A. Multi-Weyl topological semimetals stabilized by point group symmetry. *Phys. Rev. Lett.* **108**, 266802. https://doi.org/10.1103/PhysRevLett.108.266802 (2012).
5. Dantas, R., Pena-Benitez, F., Roy, B. & Surówka, P. Magnetotransport in multi-Weyl semimetals: A kinetic theory approach. *J. High Energy Phys.* **2018**, 1. https://doi.org/10.1007/JHEP12(2018)069 (2018).
6. Nielsen, H. & Ninomiya, M. A no-go theorem for regularizing chiral fermions. *Phys. Lett. B* **105**, 219. https://doi.org/10.1016/0370-2693(81)91026-1 (1981).
7. Huang, X. *et al.* Observation of the chiral-anomaly-induced negative magnetoresistance in 3d Weyl semimetal TaAs. *Phys. Rev. X* **5**, 031023. https://doi.org/10.1103/PhysRevX.5.031023 (2015).
8. Lv, B. Q. *et al.* Experimental discovery of Weyl semimetal TaAs. *Phys. Rev. X* **5**, 031013. https://doi.org/10.1103/PhysRevX.5.031013 (2015).
9. Xu, S.-Y. *et al.* Discovery of a Weyl fermion semimetal and topological Fermi arcs. *Science* **349**, 613. https://doi.org/10.1126/science.aaa9297 (2015).
10. Ruan, J. *et al.* Symmetry-protected ideal Weyl semimetal in HgTe-class materials. *Nat. Commun.* **7**, 11136. https://doi.org/10.1038/ncomms11136 (2016).
11. Xu, G., Weng, H., Wang, Z., Dai, X. & Fang, Z. Chern semimetal and the quantized anomalous Hall effect in $HgCr_2Se_4$. *Phys. Rev. Lett.* **107**, 186806. https://doi.org/10.1103/PhysRevLett.107.186806 (2011).
12. Huang, S.-M. *et al.* New type of Weyl semimetal with quadratic double weyl fermions. *Proc. Natl. Acad. Sci.* **113**, 1180. https://doi.org/10.1073/pnas.1514581113 (2016).
13. Singh, B. *et al.* Tunable double-Weyl fermion semimetal state in the $SrSi_2$ materials class. *Sci. Rep.* **8**, 10540. https://doi.org/10.1038/s41598-018-28644-y (2018).
14. Liu, Q. & Zunger, A. Predicted realization of cubic Dirac fermion in quasi-one-dimensional transition-metal monochalcogenides. *Phys. Rev. X* **7**, 021019. https://doi.org/10.1103/PhysRevX.7.021019 (2017).
15. Son, D. T. & Spivak, B. Z. Chiral anomaly and classical negative magnetoresistance of Weyl metals. *Phys. Rev. B* **88**, 104412. https://doi.org/10.1103/PhysRevB.88.104412 (2013).
16. Burkov, A. A. Giant planar Hall effect in topological metals. *Phys. Rev. B* **96**, 041110. https://doi.org/10.1103/PhysRevB.96.041110 (2017).
17. Li, Y. *et al.* Negative magnetoresistance in Weyl semimetals NbAs and NbP: Intrinsic chiral anomaly and extrinsic effects. *Front. Phys.* **12**, 127205. https://doi.org/10.1007/s11467-016-0636-8 (2017).
18. Nandy, S., Sharma, G., Taraphder, A. & Tewari, S. Chiral anomaly as the origin of the planar Hall effect in Weyl semimetals. *Phys. Rev. Lett.* **119**, 176804. https://doi.org/10.1103/PhysRevLett.119.176804 (2017).
19. Nandy, S., Taraphder, A. & Tewari, S. Berry phase theory of planar Hall effect in topological insulators. *Sci. Rep.* **8**, 14983. https://doi.org/10.1038/s41598-018-33258-5 (2018).
20. Nag, T. & Nandy, S. Magneto-transport phenomena of type-I multi-Weyl semimetals in co-planar setups. *J. Phys. Condens. Matter* **33**, 075504. https://doi.org/10.1088/1361-648X/abc310 (2020).
21. Yadav, S., Fazzini, S. & Mandal, I. Magneto-transport signatures in periodically-driven Weyl and multi-Weyl semimetals. *Phys. E* **144**, 115444. https://doi.org/10.1016/j.physe.2022.115444 (2022).
22. Nielsen, H. & Ninomiya, M. The Adler-Bell-Jackiw anomaly and Weyl fermions in a crystal. *Phys. Lett. B* **130**, 389. https://doi.org/10.1016/0370-2693(83)91529-0 (1983).
23. Huang, Z.-M., Zhou, J. & Shen, S.-Q. Topological responses from chiral anomaly in multi-Weyl semimetals. *Phys. Rev. B* **96**, 085201. https://doi.org/10.1103/PhysRevB.96.085201 (2017).
24. Sharma, G., Goswami, P. & Tewari, S. Nernst and magnetothermal conductivity in a lattice model of Weyl fermions. *Phys. Rev. B* **93**, 035116. https://doi.org/10.1103/PhysRevB.93.035116 (2016).
25. Zhang, S.-B., Lu, H.-Z. & Shen, S.-Q. Linear magnetoconductivity in an intrinsic topological weyl semimetal. *New J. Phys.* **18**, 053039. https://doi.org/10.1088/1367-2630/18/5/053039 (2016).
26. Chen, Q. & Fiete, G. A. Thermoelectric transport in double-weyl semimetals. *Phys. Rev. B* **93**, 155125. https://doi.org/10.1103/PhysRevB.93.155125 (2016).
27. Das, K. & Agarwal, A. Linear magnetochiral transport in tilted type-I and type-II Weyl semimetals. *Phys. Rev. B* **99**, 085405. https://doi.org/10.1103/PhysRevB.99.085405 (2019).
28. Das, K. & Agarwal, A. Berry curvature induced thermopower in type-I and type-II Weyl semimetals. *Phys. Rev. B* **100**, 085406. https://doi.org/10.1103/PhysRevB.100.085406 (2019).
29. Das, K. & Agarwal, A. Thermal and gravitational chiral anomaly induced magneto-transport in Weyl semimetals. *Phys. Rev. Res.* **2**, 013088. https://doi.org/10.1103/PhysRevResearch.2.013088 (2020).
30. Das, S., Das, K. & Agarwal, A. Nonlinear magnetoconductivity in Weyl and multi-Weyl semimetals in quantizing magnetic field. *Phys. Rev. B* **105**, 235408. https://doi.org/10.1103/PhysRevB.105.235408 (2022).
31. Pal, O., Dey, B. & Ghosh, T. K. Berry curvature induced magnetotransport in 3d noncentrosymmetric metals. *J. Phys. Condens. Matter* **34**, 025702. https://doi.org/10.1088/1361-648X/ac2fd4 (2022).
32. Pal, O., Dey, B. & Ghosh, T. K. Berry curvature induced anisotropic magnetotransport in a quadratic triple-component fermionic system. *J. Phys. Condens. Matter* **34**, 155702. https://doi.org/10.1088/1361-648X/ac4cee (2022).
33. Fu, L. X. & Wang, C. M. Thermoelectric transport of multi-Weyl semimetals in the quantum limit. *Phys. Rev. B* **105**, 035201. https://doi.org/10.1103/PhysRevB.105.035201 (2022).
34. Araki, Y. Magnetic textures and dynamics in magnetic Weyl semimetals. *Ann. Phys.* **532**, 1900287. https://doi.org/10.1002/andp.201900287 (2020).
35. Mizuta, Y. P. & Ishii, F. Contribution of Berry curvature to thermoelectric effects. *Proc. Int. Conf. Strong. Correl. Electron Syst. (SCES2013)* **3**, 017035. https://doi.org/10.7566/JPSCP.3.017035 (2014).
36. Knoll, A., Timm, C. & Meng, T. Negative longitudinal magnetoconductance at weak fields in Weyl semimetals. *Phys. Rev. B* **101**, 201402. https://doi.org/10.1103/PhysRevB.101.201402 (2020).
37. Medel Onofre, L. & Martín-Ruiz, A. Planar hall effect in Weyl semimetals induced by pseudoelectromagnetic fields. *Phys. Rev. B* **108**, 155132. https://doi.org/10.1103/PhysRevB.108.155132 (2023).
38. Ghosh, R. & Mandal, I. Electric and thermoelectric response for Weyl and multi-Weyl semimetals in planar Hall configurations including the effects of strain. *Physica E* **159**, 115914. https://doi.org/10.1016/j.physe.2024.115914 (2024).

39. Ghosh, R. & Mandal, I. Direction-dependent conductivity in planar Hall set-ups with tilted Weyl/multi-Weyl semimetals. *J. Phys. Condens. Matter* **36**, 275501. https://doi.org/10.1088/1361-648X/ad38fa (2024).
40. Li, L., Cao, J., Cui, C., Yu, Z.-M. & Yao, Y. Planar Hall effect in topological Weyl and nodal-line semimetals. *Phys. Rev. B* **108**, 085120. https://doi.org/10.1103/PhysRevB.108.085120 (2023).
41. Guinea, F., Katsnelson, M. I. & Geim, A. Energy gaps and a zero-field quantum Hall effect in graphene by strain engineering. *Nat. Phys.* **6**, 30. https://doi.org/10.1038/nphys1420 (2010).
42. Guinea, F., Geim, A. K., Katsnelson, M. I. & Novoselov, K. S. Generating quantizing pseudomagnetic fields by bending graphene ribbons. *Phys. Rev. B* **81**, 035408. https://doi.org/10.1103/PhysRevB.81.035408 (2010).
43. Low, T. & Guinea, F. Strain-induced pseudomagnetic field for novel graphene electronics. *Nano Lett.* **10**, 3551. https://doi.org/10.1021/nl1018063 (2010).
44. Cortijo, A., Ferreirós, Y., Landsteiner, K. & Vozmediano, M. A. H. Elastic gauge fields in Weyl semimetals. *Phys. Rev. Lett.* **115**, 177202. https://doi.org/10.1103/PhysRevLett.115.177202 (2015).
45. Liu, C.-X., Ye, P. & Qi, X.-L. Chiral gauge field and axial anomaly in a Weyl semimetal. *Phys. Rev. B* **87**, 235306. https://doi.org/10.1103/PhysRevB.87.235306 (2013).
46. Pikulin, D. I., Chen, A. & Franz, M. Chiral anomaly from strain-induced gauge fields in Dirac and Weyl semimetals. *Phys. Rev. X* **6**, 041021. https://doi.org/10.1103/PhysRevX.6.041021 (2016).
47. Arjona, V. & Vozmediano, M. A. Rotational strain in Weyl semimetals: A continuum approach. *Phys. Rev. B* **97**, 201404. https://doi.org/10.1103/PhysRevB.97.201404 (2018).
48. Ghosh, S., Sinha, D., Nandy, S. & Taraphder, A. Chirality-dependent planar Hall effect in inhomogeneous Weyl semimetals. *Phys. Rev. B* **102**, 121105. https://doi.org/10.1103/PhysRevB.102.121105 (2020).
49. Ahmad, A., Raman, K. V., Tewari, S. & Sharma, G. Longitudinal magnetoconductance and the planar Hall conductance in inhomogeneous Weyl semimetals. *Phys. Rev. B* **107**, 144206. https://doi.org/10.1103/PhysRevB.107.144206 (2023).
50. Kamboj, S. *et al.* Generation of strain-induced pseudo-magnetic field in a doped type-II Weyl semimetal. *Phys. Rev. B* **100**, 115105. https://doi.org/10.1103/PhysRevB.100.115105 (2019).
51. Xiao, D., Chang, M.-C. & Niu, Q. Berry phase effects on electronic properties. *Rev. Mod. Phys.* **82**, 1959. https://doi.org/10.1103/RevModPhys.82.1959 (2010).
52. Sundaram, G. & Niu, Q. Wave-packet dynamics in slowly perturbed crystals: Gradient corrections and Berry-phase effects. *Phys. Rev. B* **59**, 14915. https://doi.org/10.1103/PhysRevB.59.14915 (1999).
53. Xiao, D., Yao, W. & Niu, Q. Valley-contrasting physics in graphene: Magnetic moment and topological transport. *Phys. Rev. Lett.* **99**, 236809. https://doi.org/10.1103/PhysRevLett.99.236809 (2007).
54. Könye, V. & Ogata, M. Microscopic theory of magnetoconductivity at low magnetic fields in terms of Berry curvature and orbital magnetic moment. *Phys. Rev. Res.* **3**, 033076. https://doi.org/10.1103/PhysRevResearch.3.033076 (2021).
55. Nag, T., Menon, A. & Basu, B. Thermoelectric transport properties of Floquet multi-Weyl semimetals. *Phys. Rev. B* **102**, 014307.https://doi.org/10.1103/PhysRevB.102.014307 (2020).
56. Watzman, S. J. *et al.* Dirac dispersion generates unusually large Nernst effect in Weyl semimetals. *Phys. Rev. B* **97**, 161404. https://doi.org/10.1103/PhysRevB.97.161404 (2018).
57. Ashcroft, N. & Mermin, N. *Solid State Physics* (Cengage Learning, 2011) https://books.google.de/books?id=x_s_YAAACAAJ.
58. Mandal, I. & Saha, K., Thermoelectric response in nodal-point semimetals, arXiv e-prints (2023), arXiv:2309.10763 [cond-mat.mes-hall].
59. Xiao, D., Yao, Y., Fang, Z. & Niu, Q. Berry-phase effect in anomalous thermoelectric transport. *Phys. Rev. Lett.* **97**, 026603. https://doi.org/10.1103/PhysRevLett.97.026603 (2006).
60. Li, Q. *et al.* Chiral magnetic effect in $ZrTe_5$. *Nat. Phys.* **12**, 550. https://doi.org/10.1038/nphys3648 (2016).
61. Zhang, C.-L. *et al.* Signatures of the Adler-Bell-Jackiw chiral anomaly in a Weyl fermion semimetal. *Nat. Commun.* **7**, 10735. https://doi.org/10.1038/ncomms10735 (2016).
62. Shama, G. R. & Singh, Y. Observation of planar Hall effect in the ferromagnetic Weyl semimetal $Co_3Sn_2S_2$. *J. Magn. Magn. Mater.* **502**, 166547. https://doi.org/10.1016/j.jmmm.2020.166547 (2020).
63. Tanwar, P. K. *et al.* Gravitational anomaly in the ferrimagnetic topological Weyl semimetal NdAlSi. *Phys. Rev. B* **108**, L161106. https://doi.org/10.1103/PhysRevB.108.L161106 (2023).
64. Diaz, J. *et al.* Bending strain in 3D topological semi-metals. *J. Phys. D Appl. Phys.* **55**, 084001. https://doi.org/10.1088/1361-6463/ac357f (2021).
65. Ghosh, R., Haidar, F. & Mandal, I. arXiv e-prints (2024), arXiv:2408.01422[cond-mat.mes-hall].
66. Mandal, I. & Saha, K. Thermopower in an anisotropic two-dimensional Weyl semimetal. *Phys. Rev. B* **101**, 045101. https://doi.org/10.1103/PhysRevB.101.045101 (2020).
67. Stålhammar, M., Larana-Aragon, J., Knolle, J. & Bergholtz, E. J. Magneto-optical conductivity in generic Weyl semimetals. *Phys. Rev. B* **102**, 235134. https://doi.org/10.1103/PhysRevB.102.235134 (2020).
68. Yadav, S., Sekh, S. & Mandal, I. Magneto-optical conductivity in the type-I and type-II phases of Weyl/multi-Weyl semimetals. *Physica B* **656**, 414765. https://doi.org/10.1016/j.physb.2023.414765 (2023).
69. Mandal, I. & Gemsheim, S. Emergence of topological Mott insulators in proximity of quadratic band touching points. *Condens. Matter Phys.* **22**, 13701. https://doi.org/10.5488/CMP.22.13701 (2019).
70. Mandal, I. Effect of interactions on the quantization of the chiral photocurrent for double-Weyl semimetals. *Symmetry* **12**, 919 (2020).
71. Mandal, I. Robust marginal Fermi liquid in birefringent semimetals. *Phys. Lett. A* **418**, 127707. https://doi.org/10.1016/j.physleta.2021.127707 (2021).
72. Mandal, I. & Ziegler, K. Robust quantum transport at particle-hole symmetry. *EPL (Europhysics Letters)* **135**, 17001. https://doi.org/10.1209/0295-5075/ac1a25 (2021).
73. Nandkishore, R. M. & Parameswaran, S. A. Disorder-driven destruction of a non-Fermi liquid semimetal studied by renormalization group analysis. *Phys. Rev. B* **95**, 205106. https://doi.org/10.1103/PhysRevB.95.205106 (2017).
74. Mandal, I. & Nandkishore, R. M. Interplay of Coulomb interactions and disorder in three-dimensional quadratic band crossings without time-reversal symmetry and with unequal masses for conduction and valence bands. *Phys. Rev. B* **97**, 125121. https://doi.org/10.1103/PhysRevB.97.125121 (2018).
75. Mandal, I. Fate of superconductivity in three-dimensional disordered Luttinger semimetals. *Ann. Phys.* **392**, 179. https://doi.org/10.1016/j.aop.2018.03.004 (2018).
76. Mandal, I. & Freire, H. Transport properties in non-Fermi liquid phases of nodal-point semimetals, arXiv e-prints (2024), arXiv:2404.08635 [cond-mat.str-el]
77. Bera, S. & Mandal, I. Floquet scattering of quadratic band-touching semimetals through a time-periodic potential well. *J. Phys. Condens. Matter* **33**, 295502. https://doi.org/10.1088/1361-648X/ac020a (2021).
78. Bera, S., Sekh, S. & Mandal, I. Floquet transmission in Weyl/multi-Weyl and nodal-line semimetals through a time-periodic potential well. *Ann. Phys. (Berlin)* **535**, 2200460. https://doi.org/10.1002/andp.202200460 (2023).

Acknowledgements
LM and AMR acknowledge support from CONACyT (México) under project number CF- 428214, and DGAPA-UNAM under project number AG100224. IM's research has received funding from the European Union's Horizon 2020 research and innovation programme under the Marie Skłodowska-Curie grant agreement number 754340.

Author contributions
L.M. did the calculations. I.M. perceived the idea, wrote the main manuscript text, analyzed the results, and prepared the figures. R.G. helped in some of the calculations. A.M.-R. reviewed the write-up. All authors reviewed the manuscript.

Competing interests
The authors declare no competing interests.

Additional information
Supplementary Information The online version contains supplementary material available at https://doi.org/10.1038/s41598-024-68615-0.

Correspondence and requests for materials should be addressed to L.M.

Reprints and permissions information is available at www.nature.com/reprints.

Publisher's note Springer Nature remains neutral with regard to jurisdictional claims in published maps and institutional affiliations.